NRC Publications Archive
Archives des publications du CNRC

A Gemini/GMOS study of intermediate luminosity early-type Virgo cluster galaxies. I. Globular cluster and stellar kinematics

Li, Biao; Peng, Eric W.; Zhang, Hong-xin; Blakeslee, John P.; Côté, Patrick J D (Pat); Ferrarese, Laura; Jordán, Andrés; Liu, Chengze; Mei, Simona; Puzia, Thomas H.; Takamiya, Marianne; Trancho, Gelys; West, Michael J.

NRC Publications Record / Notice d'Archives des publications de CNRC:
https://nrc-publications.canada.ca/eng/view/object/?id=40e943c3-ac42-409c-a4df-e2aede52aed6
https://publications-cnrc.canada.ca/fra/voir/objet/?id=40e943c3-ac42-409c-a4df-e2aede52aed6

National Research Council Canada   Conseil national de recherches Canada

Canada

A GEMINI/GMOS STUDY OF INTERMEDIATE LUMINOSITY EARLY-TYPE VIRGO CLUSTER GALAXIES. I. GLOBULAR CLUSTER AND STELLAR KINEMATICS

BIAO LI[1,2], ERIC W. PENG[1,2], HONG-XIN ZHANG[1,2,3,4,6,15], JOHN P. BLAKESLEE[5], PATRICK CÔTÉ[5], LAURA FERRARESE[5],
ANDRÉS JORDÁN[6,7], CHENGZE LIU[8,9], SIMONA MEI[10,11], THOMAS H. PUZIA[6], MARIANNE TAKAMIYA[12], GELYS TRANCHO[13], AND
MICHAEL J. WEST[14]

[1] Department of Astronomy, Peking University, Beijing 100871, China; biaolee@pku.edu.cn, peng@pku.edu.cn
[2] Kavli Institute for Astronomy and Astrophysics, Peking University, China
[3] Chinese Academy of Sciences South America Center for Astronomy, Camino EI Observatorio #1515, Las Condes, Santiago, Chile
[4] National Astronomical Observatories, Chinese Academy of Sciences, Beijing 100012, China
[5] National Research Council of Canada, Herzberg Astronomy and Astrophysics Program, 5071 West Saanich Road, Victoria, BC V9E 2E7, Canada
[6] Instituto de Astrofísica, Facultad de Física, Pontificia Universidad Católica de Chile, Av.Vicuña Mackenna 4860, 7820436 Macul, Santiago, Chile
[7] Millennium Institute of Astrophysics, Av.Vicuña Mackenna 4860, 7820436 Macul, Santiago, Chile
[8] Department of Physics, Shanghai Jiao Tong University, 800 Dongchuan Road, Shangai 200240, China
[9] Shanghai Key Lab for Particle Physics and Cosmology, Shanghai Jiao Tong University, Shanghai 200240, China
[10] GEPI, Observatoire de Paris, PSL Research Institute CNRS, University of Paris Diderot, 61, Avenue de l'Observatoire 75014, Paris, France
[11] Université Paris Denis Diderot, Université Paris Sorbonne Cité, F-75205 Paris Cedex 13, France
[12] Institute for Astronomy, University of Hawaii, 2680 Woodlawn Dr., Honolulu, HI 96822, USA
[13] Giant Magellan Telescope Organization, 251 South Lake Avenue, Pasadena, CA 91101, USA
[14] Maria Mitchell Observatory, 4 Vestal Street, Nantucket, MA, 02554, USA

ABSTRACT

We present a kinematic analysis of the globular cluster (GC) systems and diffuse stellar light of four intermediate luminosity (sub-L^*) early-type galaxies in the Virgo cluster based on Gemini Multi-Object Spectrographs (GMOS) data. Our galaxy sample is fainter ($-23.8 < M_K < -22.7$) than most previous studies, nearly doubling the number of galaxies in this magnitude range that now have GC kinematics. The data for the diffuse light extends to $4R_e$, and the data for the GCs reaches 8–$12R_e$. We find that the kinematics in these outer regions are all different despite the fact that these four galaxies have similar photometric properties, and are uniformly classified as "fast rotators" from their stellar kinematics within $1R_e$. The GC systems exhibit a wide range of kinematic morphology. The rotation axis and amplitude can change between the inner and outer regions, including a case of counter-rotation. This difference shows the importance of wide-field kinematic studies, and shows that stellar and GC kinematics can change significantly as one moves beyond the inner regions of galaxies. Moreover, the kinematics of the GC systems can differ from that of the stars, suggesting that the formation of the two populations are also distinct.

Key words: galaxies: elliptical and lenticular, cD – galaxies: kinematics and dynamics – galaxies: star clusters: general

1. INTRODUCTION

Early-type galaxies (ETGs) are thought to be the final products of mergers and accretion processes in a hierarchical universe. This history of collapse and merging is preserved in the motions of their stars. Stellar kinematics can therefore be used to constrain galactic formation and evolution. Absorption line profiles measured from integrated spectroscopy can measure these bulk stellar motions. However, these observations are usually restricted to within 1–2 effective radii ($R \lesssim 1$–$2R_e$) of galaxy centers (Gerhard et al. 2001; Pinkney et al. 2003; Proctor et al. 2005; Spolaor et al. 2008) due to the faintness of the stellar halo. With the development of integral field units (IFUs), this technique has given us a new two-dimensional (2D) view of the line-of-sight velocity distribution in galaxies (Bacon et al. 2001; Cappellari et al. 2011; Sánchez et al. 2012; Emsellem et al. 2014; Bundy et al. 2015; Guérou et al. 2015). Cappellari et al. (2011) observed 260 ETGs in the nearby universe with the Spectrographic Areal Unit for Research on Optical Nebulae (SAURON) IFU in the ATLAS[3D] project. They were able to measure the projected angular momentum per unit mass, and used this parameter to

classify 260 ETGs as either "fast" or "slow" rotators, finding that nearly all but the most massive ETGs are fast rotators (Emsellem et al. 2011). They argue for a shift in the existing paradigm for ETGs, where galaxies generally classified morphologically into disc-like S0 galaxies and spheroidal-like E systems should instead be classified kinematically.

However, like earlier studies, the ATLAS[3D] project is limited to $1R_e$, where relaxation processes make inferring formation histories increasingly difficult, and where feedback processes complicate things even further. The fraction of the total mass in this region may only be ~15%–30% (Wu et al. 2014). In addition, the outer regions may present more obvious signatures of merging or accretion events. There are only a few studies that extend out to ~2–$4R_e$ (Mehlert et al. 2000; Proctor et al. 2009; Weijmans et al. 2009; Forestell & Gebhardt 2010; Arnold et al. 2014). Proctor et al. (2009) developed a new technique for extracting integrated spectra of the field stars, or galaxy diffuse light (GDL), contained in multi-slit observations, and found a variety of rotation profiles beyond $1R_e$ for five ETGs. They found that the stellar kinematics in their galaxies' inner regions were not necessarily predictive of those in the outer regions. One possibility is that dissipation processes in gas-rich major mergers produce

---
[15] CAS-CONICYT Fellow.

ID	Type	R.A.(J2000) (deg)	decl.(J2000) (deg)	V_{sys} (km s^{-1})	R_e (kpc)	D (Mpc)	M_K (mag)	PA$_K$ (degree)	$(b/a)_K$
(1)	(2)	(3)	(4)	(5)	(6)	(7)	(8)	(9)	(10)
VCC1231 (NGC4473)	E5	187.453659	+13.429320	2260	1.2	15.2	−23.77	275	0.54
VCC2000 (NGC4660)	E5	191.133209	+11.190533	1087	0.8	15.0	−22.69	280	0.5
VCC1062 (NGC4442)	SB0	187.016220	+09.803620	547	1.3	15.3	−23.63	82	0.51
VCC0685 (NGC4350)	SA0	185.990891	+16.693356	1210	0.9	15.4	−23.13	30	0.3

Note. Hubble types (2) are from the NED database. The position of galaxy center, R.A. (3) and decl. (4), the galaxy systemic velocity (5) and the K-band absolute magnitude (8) are all from ATLAS^{3D} project (Cappellari et al. 2011), where (8) are derived from the 2MASS extended source catalog (Jarrett et al. 2000). The effective radii (6) are from Ferrarese et al. (2006). The distances (7) are from Blakeslee et al. (2009), except VCC 685 which is from the GC luminosity function estimates by Jordán et al. (2007). The photometric position angle (9) and axis ratio (10) are from 2MASS (Skrutskie et al. 2006).

dramatic kinematic differences between the inner and outer regions (Hoffman et al. 2010). Alternatively, the galaxies could have formed in two separate phases, with the inner region forming early by dissipation, and the outer region forming later by accretion of smaller galaxies (Oser et al. 2010). Further studying stellar kinematics at large radius is clearly an important direction to pursue.

Compared to stellar kinematics, which are limited by low surface brightness, observations of globular clusters (GCs) can extend out to much larger distances ($\sim 10R_e$) from the galaxy center. Because GCs are compact and luminous, they are easily observed in the halos of galaxies. GCs are old, coeval collections of stars that can survive a Hubble time, and they preserve information on the assembly history of their host galaxies.

In recent years, large samples of GC velocities around ETGs have been produced (e.g., M87, Strader et al. 2011; NGC 1399, Schuberth et al. 2010; NGC 5128, Peng et al. 2004b, Woodley et al. 2010). For practical reasons, much of the work in this field has focused on massive ETGs and their rich GC systems. ETGs at intermediate mass, however, are much more common, and perhaps less complicated than their more massive counterparts. For these ETGs, with luminosities at or fainter than the knee of the galaxy luminosity function ($M_K = -24.2$ mag, Cole et al. 2001, $h = 0.7$), there are only a few studies (NGC 3115, Arnold et al. 2011; NGC 3379, Puzia et al. 2004, Pierce et al. 2006, Bergond et al. 2006; NGC 4494, Foster et al. 2011; NGC 821, 3377, 1400, 4278, 7454, Pota et al. 2013). Due to lower surface brightnesses and sparser GC systems, these galaxies generally lack kinematic data at large radii.

Romanowsky et al. (2003) and Douglas et al. (2007) used planetary nebulae as kinematic tracers and found some intermediate luminosity ETGs (NGC 3379, NGC 821, and NGC 4494) with low mass-to-light ratios, which appeared to conflict with the dark matter fractions predicted in cosmological simulations. Compared to massive ETGs, intermediate luminosity ETGs may also have more sporadic merger histories with different mass ratios, potentially preserving the wide range of assembly processes at work, and making them important and interesting targets of study.

In this paper, we study the GC and stellar kinematics of four intermediate luminosity ETGs in the Virgo cluster out to large radii. We compare GC and stellar kinematic trends (rotation amplitude and position angle (PA)) with each other, and at different radii. In our next paper (B. Li et al., 2015, in

preparation), we will study the mass distribution and dark matter content of these intermediate luminosity ETGs.

2. SAMPLE, OBSERVATIONS, AND DATA

2.1. Sample

We selected four intermediate-luminosity ETGs from the ACS Virgo Cluster Survey (ACSVCS; Côté et al. 2004), a homogeneous Hubble Space Telescope survey of 100 ETGs in the nearby Virgo cluster of galaxies using the Advanced Camera for Surveys (ACS; Ford et al. 1998). These deep images, with their high spatial resolution, allow for excellent selection of GCs (Jordán et al. 2009). This is crucial for our sample galaxies, as they do not have very rich GC systems, and contamination from foreground and background sources can significantly reduce the spectroscopic yield.

The four galaxies in our study are VCC 1231, 2000, 1062, and 685 (NGC 4473, 4660, 4442, and 4350, respectively, see Table 1). They span the interesting L^* to sub-L^* luminosity range ($-20.5 < M_B < -19$), making them fainter than galaxies targted in typical GC kinematic studies. For its luminosity range, this sample now doubles the number of galaxies with GC kinematics. According to NED, two have morphological type E5, and the other two are classified as S0. All galaxies are classified as "fast rotators" by ATLAS^{3D} (Emsellem et al. 2011).

2.2. Observation

We observed these galaxies with the Gemini Multi-Object Spectrographs (GMOS, Hook et al. 2004), twin instruments on the Gemini North and Gemini South telescopes. Our target galaxies have sizes ($R_e \sim 10$–$18''$) that fit well within the GMOS field of view (5.5 arcmin^2), providing coverage out to 10–16R_e. Each galaxy contained ~ 50 targetable GCs with $V < 23$ mag. VCC 1231, VCC 1062, and VCC 2000 data were taken with GMOS-South, whereas data for VCC 685 was taken with GMOS-North. We observed three masks for each galaxy to overcome the issue of slit-crowding at the galaxy centers. VCC 685 was only observed with one mask due to it being lower priority in the queue. Table 2 summarizes the observing information. Because there are two gaps in the GMOS CCD focal plane, we observed with two wavelength centers, 5080 and 5120 Å, dithering exposures between the two. For each central wavelength, we took two exposures. We used the B600_G5323(GMOS North) and B600_5303(GMOS South) grisms with 1″0 wide slits, giving a dispersion of 0.5 and

<div align="center">

Table 2
Summary of Gemini/MOS Observation

</div>

Mask	R.A.(J2000) (deg)	Decl.(J2000) (deg)	Exp.Time (seconds)	Slits	Night
GS2008AQ008–01	191.134109	+11.176211	3040	22	2008 Apr 06
GS2008AQ008–02	191.134109	+11.176211	3040	23	2008 Apr 07
GS2008AQ008–03	191.134109	+11.176211	3040	20	2008 Apr 08
GS2008AQ008–04	187.453537	+13.427367	3040	30	2008 Mar 14
GS2008AQ008–05	187.453537	+13.427367	3040	25	2008 Apr 01
GS2008AQ008–06	187.453537	+13.427367	3040	27	2008 Apr 05
GS2008AQ008–07	187.024216	+09.806433	2700	21	2008 Mar 02
GS2008AQ008–08	187.024216	+09.806433	2700	21	2008 Mar 09
GS2008AQ008–09	187.024216	+09.806433	2700	21	2008 Mar 14
GN2008AQ073–01	186.002594	+16.686339	2820	24	2008 Mar 31

$0.45\,\text{Å pixel}^{-1}$, respectively. Both grisms give a spectral resolution of $R = 1688$. (Puzia et al. 2013)

2.3. Data Reduction

The data reduction was performed by using the Gemini/GMOS IRAF package (Version 1.11). (1) The cosmic ray rejection was done using the GSCRSPEC script, which was originally written by Bryan Mlller. GSCRSPEC is an MEF wrapper for the spectroscopic version of the Laplacian Cosmic Ray Identification routine (van Dokkum 2001). (2) The bias subtraction and flat-fielding were done by the GSDEDUCE. (3) We used GSWAVELENGTH to establish the wavelength calibration from the CuAr arc frames. Typical wavelength solution residuals were ~ 0.1–0.3Å. (4) The wavelength calibration was applied to the object frames by using GSTRANSFORM. (5) We used GSSKYSUB to do the sky-subtracted interactively and GSEXTRACT to extract 1D spectra from each object frame. (6) Finally, we used the SCOMBINE to median combine extracted spectra from the same slits.

After extracting the target spectrum from each of the mask slitlets, we get a "background" spectrum for each slitlets. For slits closer to the galaxy center, this "background" spectrum contains not only sky but also useful amounts of host GDL. If the slit is far from the galaxy center, the spectrum should be dominated by "pure sky." In order to recover information from the slits with significant amounts of galaxy light, we carefully choose slits at the greatest distance ($\sim 7 R_e$) from the galaxy center and combine their spectra to produce a pure sky spectrum for non-local sky subtraction. We do not use slits located near the edges of the mask where the vignetting effects are serious. After subtracting the sky spectrum from the remaining "background" spectra we are left with the GDL spectra. Figure 1 shows GC and GDL spectra with different signal-to-noise ratio (S/N). Our spectra typically cover a wavelength range from 3500 to 6500 Å, but the wavelength range depends on the slit position on the mask and some spectra can reach wavelengths as red as 7200 Å.

2.4. Radial Velocity Determination

We use the FXCOR task in IRAF to measure the GC and GDL velocities. The template we use for FXCOR is a K-type M31 GC spectrum from a list of SAO spectral templates. For the GDL, we also use the penalized pixel-fitting method (pPXF) as implemented by Cappellari & Emsellem (2004) to measure radial velocities and velocity dispersions. For pPXF,
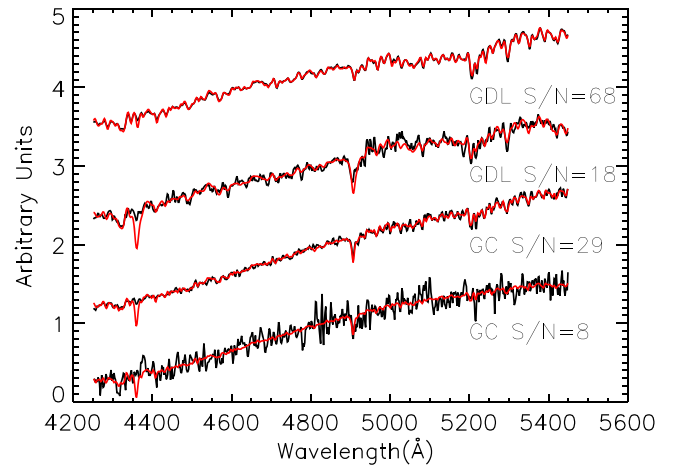

Figure 1. Reduced GC and GDL spectra. The red lines are the best-fitt PPXF templates. The S/N is calculated from 4500 to 4750 Å.

we use the MILES library of stellar spectra as templates (Sánchez-Blázquez et al. 2006). The radial velocities measured using FXCOR and pPXF are very consistent, so we choose to use the FXCOR velocities. The velocity uncertainties are estimated by FXCOR and scaled to those determined with repeated measurements of science targets. For velocity dispersion, we use the region of 4850 to 5350 Å which contains the Hβ, Mg b and Fe5270 spectroscopic features. To be conservative, we only measure the velocity dispersion within $3R_e$. The S/N of the spectra are typically too low to measure accurately the velocity dispersion in the outer regions.

We divide our GCs into red and blue populations according to the $(g - z)_0$ color distributions in Peng et al. (2006). The colors of GCs are from the ACSVCS and the Next Generation Virgo Survey (NGVS, Ferrarese et al. 2012). The NGVS data are used for objects that fall outside the ACS field of view. The transformation that we use between the ACSVCS and NGVS filters are:

$$g_{\text{ACS}} - g_{\text{NGVS}} = 0.12 \pm 0.06 \tag{1}$$

$$z_{\text{ACS}} - z_{\text{NGVS}} = -0.06 \pm 0.10. \tag{2}$$

The number of spectroscopically confirmed blue and red GCs in our galaxy sample is listed in Table 3. Most of the GCs belonging to VCC 685 and VCC 2000 are blue.

In addition to the Gemini/GMOS spectra of the GCs and GDL, all four of our sample galaxies have published IFU

Table 3
All GC Kinematics Fitting Results

ID	N_{blue}	N_{red}	V_m (km s^{-1})	V_{rot} (km s^{-1})	Bias (km s^{-1})	σ (km s^{-1})	V_{rot}/σ	PA$_{kin}$ (degree)
(1)	(2)	(3)	(4)	(5)	(6)	(7)	(8)	(9)
VCC1231	39	12	2268	35 ± 40	31	171 ± 24	0.2 ± 0.2	216 ± 78
VCC2000	42	1	1062	100 ± 42	5	128 ± 20	0.8 ± 0.4	198 ± 32
VCC1062	28	12	484	153 ± 28	8	108 ± 18	1.4 ± 0.4	92 ± 12
VCC685	15	0	1244	66 ± 120	106	195 ± 45	0.3 ± 0.6	92 ± 91

Note. GC kinematics results for our galaxy sample. The number of blue GCs, red GCs, the mean velocity, rotation velocity (amplitude), bias of the rotation velocity, velocity dispersion, dominance parameter (V_{rot}/σ), and kinematic position angle (PA) are shown in columns (2) to (9), respectively. See Section 3.2 for details on the estimation of these parameters.
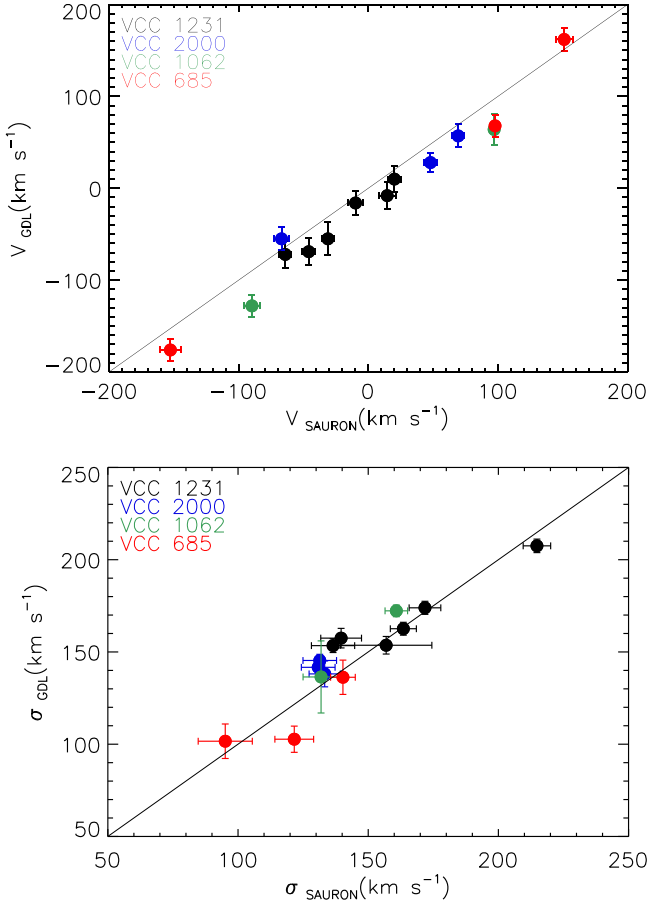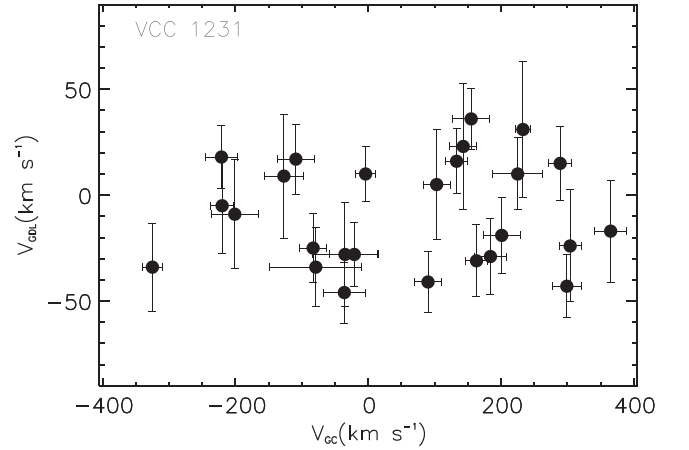

Figure 3. Velocity comparison between the GDL and the target observed in the same slits. We see the data point is random, which suggest there is no correlation between the velocity measured for the target and the GDL.

Figure 2. Comparison of our GDL radial velocity and velocity dispersion measurememts with those from the SAURON survey. Different colored data points represent difference galaxy data sets. The solid line is a 1:1 relation. The mean offset is 16 and 4 km s^{-1} for the velocity and velocity dispersion, respectively. The two surveys show good agreement.

spectroscopy from SAURON (Emsellem et al. 2004; Cappellari et al. 2011). Since we have some GDL slits in the SAURON regions, we compare our measured radial velocity and velocity dispersion with those obtained with SAURON (Figure 2). The velocities and velocity dispersions of SAURON data are from a 2D interpolation of their radial velocity and velocity dispersion field. The solid line is a 1:1 relation. We found generally good agreement between these two data sets. SAURON velocities are a little bit larger than our GDL velocities. The offset is 16 and 4 km s^{-1} for the velocity

and velocity dispersion, respectively, between our GDL data and SAURON data. To facilitate comparison to the SAURON data, we add a 16 km s^{-1} velocity offset to our measured velocities. We do not change our velocity dispersion measurements, as 4 km s^{-1} is well within the estimated uncertainties.

One possible problem of obtaining stellar kinematics with the GDL technique is that the "background" spectrum may be contaminated by residual GC light. To check whether this is a problem, we compare the velocity of the GC and GDL from the same VCC 1231 slits. In Figure 3, we show that there is no correlation between these two velocities, suggesting that the effect of the GC light on the GDL is negligible.

We present the full table of GC and GDL positions, velocities, velocity dispersions (GDL only), and uncertainties in Tables 8 and 9. The radial velocity distribution is shown in Figure 4.

3. KINEMATICS ANALYSIS

3.1. Two-dimensional Velocity Field

For each galaxy, we show the 2D velocity fields as derived from GCs (e.g., left panel of Figure 5). We use a Gaussian kernel function to smooth the velocity field. At each point, the value of the velocity field is estimated by:

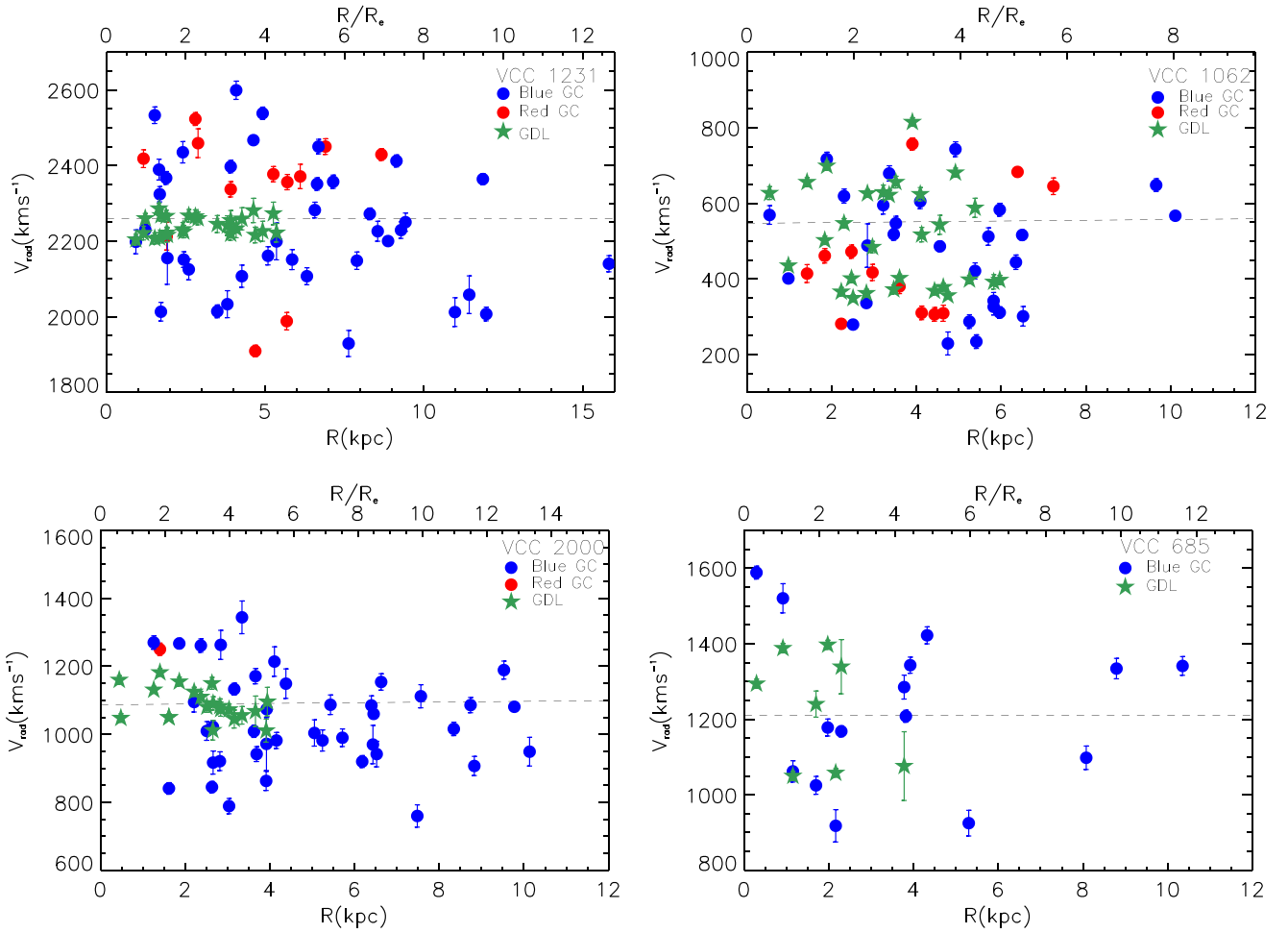$$V'(x', y') = \frac{\sum_j v_j \omega_j}{\sum_j \omega_j} \tag{3}$$

Figure 4. GC and GDL velocity distribution as function of radius. The blue, red circle, and green stars represent blue GCs, red GCs, and GDL, respectively. The galaxy systemic velocity is plotted as a dashed line.
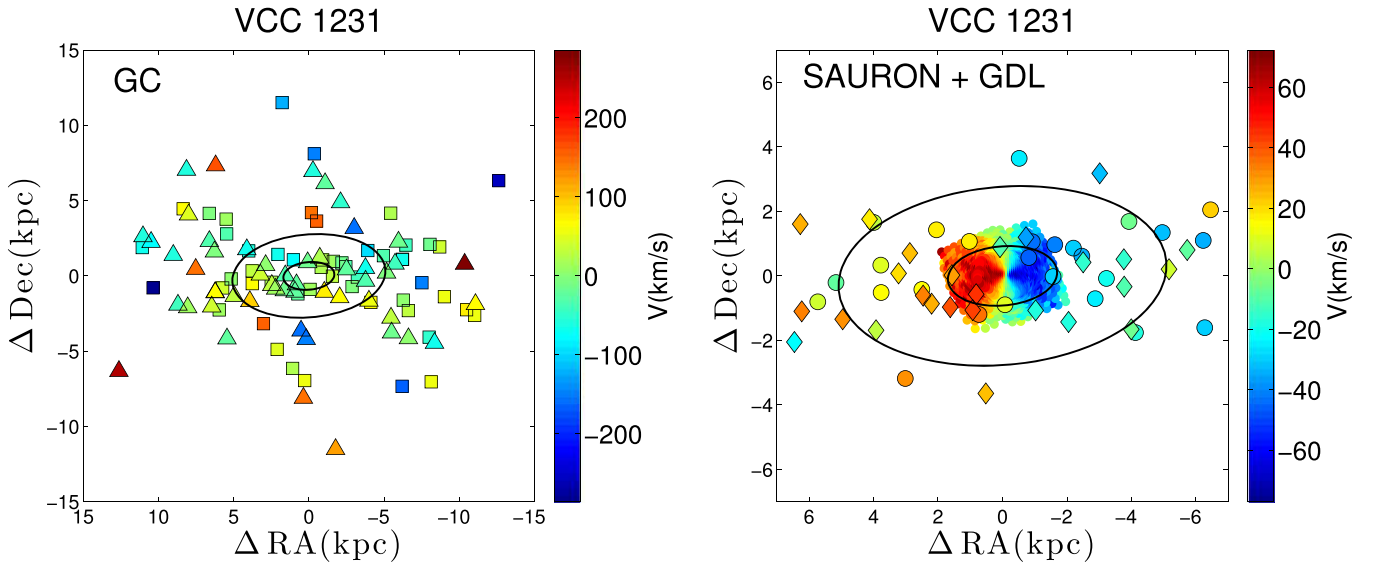
Figure 5. 2D velocity fields of our sample galaxies. Left column: smoothed GC velocity fields. Squares represent the location of the GCs, and the triangles represent the point-symmetric counterparts. The color represents the value of the smoothed velocity field at that point, with the color scale on the right hand side of each panel. The ellipses represent 1 and 3 effective radii, the values of which are listed in Table 1. Right column: stellar velocity field as derived from the GDL data without smoothing. The circles represent the location of our slits, and the diamonds represent the point-symmetric counterparts. The SAURON data are plotted in a contiguous rectangle at the galaxy center. Note that the spatial and velocity scales differ in each plot in order to best display the dynamic range. In all plots, north is up, and east is to the left.

Table 4
Blue and Red GC Kinematics Fitting Results

ID	$V_{rot,B}$ (km s^{-1})	$V_{rot,R}$ (km s^{-1})	Bias$_B$ (km s^{-1})	Bias$_R$ (km s^{-1})	σ_B (km s^{-1})	σ_R (km s^{-1})	PA$_{kin,B}$ (degree)	PA$_{kin,R}$ (degree)
(1)	(2)	(3)	(4)	(5)	(6)	(7)	(8)	(9)
VCC1231	73 ± 43	83 ± 115	21	80	157 ± 24	183 ± 51	235 ± 48	96 ± 87
VCC2000	97 ± 44	⋯	7	⋯	127 ± 20	⋯	196 ± 30	⋯
VCC1062	145 ± 37	183 ± 57	9	20	108 ± 21	104 ± 30	88 ± 16	100 ± 24

Note. Blue (B) and red (R) GC kinematics results for our galaxy sample.
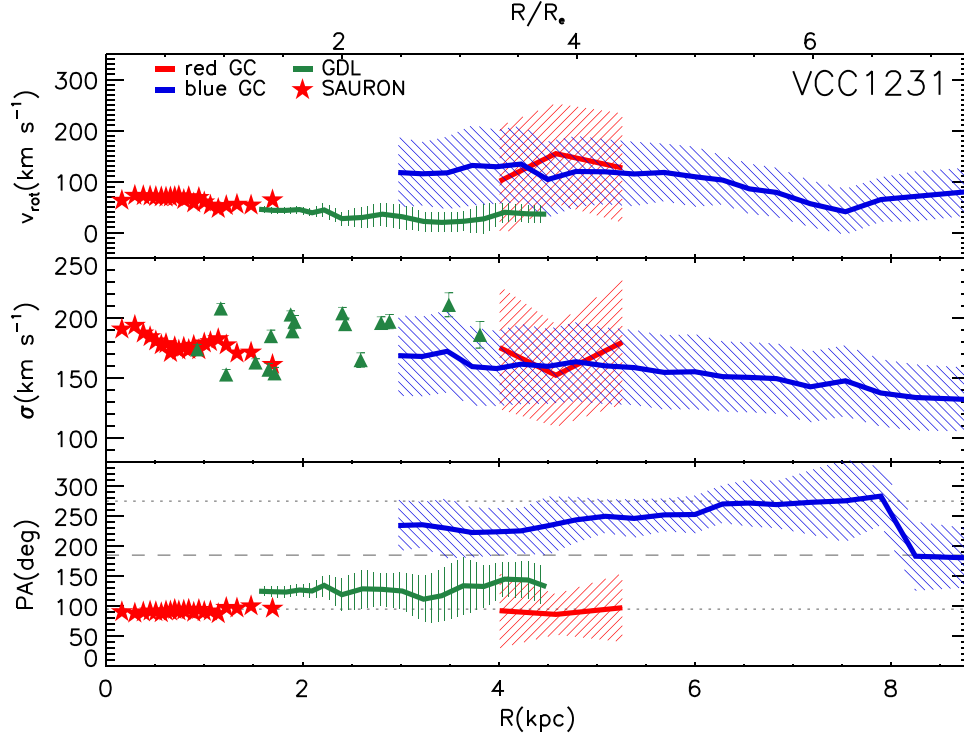

Figure 6. Kinematic fitting results as a function of radius in VCC 1231. The top panel shows the rotation amplitude. The middle panel shows the velocity dispersion. The bottom panel shows the kinematic position angle. The red stars represent the fitting results for the SAURON data. The lines represent the fitting results from the multislit galaxy diffuse light data (green line), red and blue GCs (red and blue), with the shaded regions showing the 1σ uncertainty of the fit. The green triangles represent the velocity dispersion measured in each individual slit within 3R_e. The photometric major and minor axes are represented by the dotted and dashed line in the bottom panel, respectively. The GDL measurements have a rotation axis similar to that of the SAURON data. However, the rotation amplitude (top panel) is generally lower than for the SAURON data. Red and blue GCs have the same rotation velocity but rotate around the difference axes (although with low significance). The velocity dispersion of the GDL data is consistent with that of the SAURON data. The velocity dispersion profile of blue and red GC stays flat out to large distance.

$$\omega_j = \frac{1}{\sqrt{2\pi}\sigma} \exp \frac{-D^2}{2\sigma^2} \qquad (4)$$

where ω_j depends on D, which is the distance from jth point to (x', y'), and σ which is the width of the Gaussian kernel. The Gaussian kernel can have a fixed bandwidth (Peng et al. 2004b) or vary as a function of local density (Coccato et al. 2009). The Gaussian kernel we used has a fixed width of $\sigma = 1$ kpc, which is close to 1R_e for our galaxy sample. We note that our final result is not strongly sensitive to the exact kernel width, so we choose 1 kpc as a reasonable compromise. We also found that the fixed kernel did not lead to information loss in the outer region of galaxy. In the very inner regions, where it might matter, we typically have few data points due to slit crowding.

To reduce the noise due to the finite spatial sampling of our GCs and GDL, we assume the galaxy is point-symmetric in phase space, a valid assumption for triaxial potentials. Each point (x, y, v) thus has a mirror counterpart $(-x, -y, -v)$, where the x and y are the position of the GC/GDL on the sky, and v is the radial velocity of GC/GDL minus the galaxy's systemic velocity. This technique has been adopted in Arnaboldi et al. (1998), Peng et al. (2004b), and Coccato et al. (2009). For the GCs, we plot the smoothed point-symmetric 2D velocity fields for our galaxy sample (e.g., left panel of Figure 5). For the GDL, we only plot the point-symmetric 2D velocity fields. In order to compare our GDL data to the SAURON data (Emsellem et al. 2004; Cappellari et al. 2011), we plot the SAURON data in the central regions (e.g., right panel of Figure 5). The raw radial velocity fields without smoothing, and without the assumption of point-symmetry (and hence without doubling the data) are shown in the appendix. The point-symmetric velocity fields are only used

for illustration purposes; all quantitative results in the following sections use the original, non-symmetrized data.

3.2. Rotation Amplitude and Rotation Axis

One of the main kinematic characteristics we wish to explore for halo systems is the degree of rotational support, if any. To obtain the rotation amplitude and axis for the GC systems and stars, we use methods which have been used previously (Foster et al. 2011; Strader et al. 2011; Pota et al. 2013). For this kinematic analysis, we use the original data without point-symmetric folding or smoothing. For each bin in radius, if we assume the radial velocity distribution is Gaussian, then the equivalent χ^2 is:

$$\chi^2 = \sum_i \frac{(v_i - v_{\mathrm{mod}})^2}{\sigma_p^2 + \left(\Delta v_i^2\right)} + \ln\left(\sigma_p^2 + \Delta v_i^2\right) \qquad (5)$$
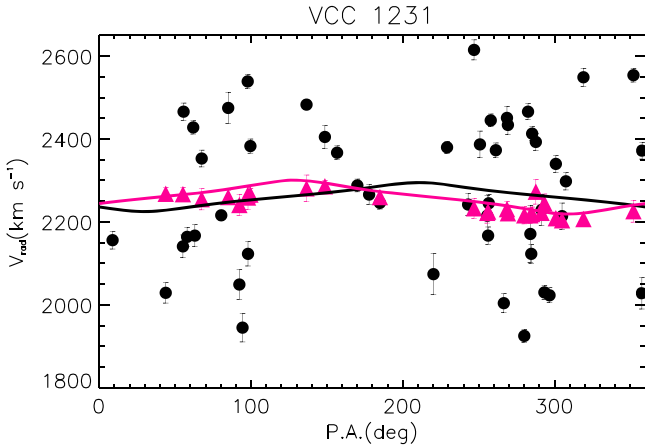

Figure 7. Radial velocities vs. position angle in VCC 1231. The black circles represent the GC data and pink triangles represent the GDL data. The black and pink solid lines represent the best-fitting rotation curve for the GCs and GDL, respectively. GCs show no rotation or very small rotation. The GDL shows small rotation. The curves are not perfect sinusoids in PA because we include the ellipticity of the system in the fit.

$$v_{\mathrm{mod}} = v_0 \pm \frac{V_{\mathrm{rot}}}{\sqrt{1 + \left(\dfrac{\tan\left(\mathrm{PA}_i - \mathrm{PA}_{\mathrm{kin}}\right)}{q_{\mathrm{kin}}}\right)^2}}, \qquad (6)$$

where v_i is the radial velocity, Δv is the velocity error, σ_p is the velocity dispersion, V_{rot} is the rotation amplitude, and v_0 is the galaxy systemic velocity. PA_i, $\mathrm{PA}_{\mathrm{kin}}$, and q_{kin} are the PA of each data point, PA of the kinematic major axis, and the kinematic axis ratio, respectively. For the GCs, we minimize the Equation (3). For the GDL, the χ_0^2 is defined as follows:

$$\chi_0^2 = \sum_i \frac{(v_i - v_{\mathrm{mod}})^2}{\left(\Delta v_i^2\right)} + \ln\left(\Delta v_i^2\right) \qquad (7)$$

For both the GCs and GDL, we assume q_{kin} is equal to the photometric axis ratio of the galaxy light since q_{kin} is difficult to constrain with our data. We also fit with $q_{\mathrm{kin}} = 1$ (round), and the results do not show any significant differences. We use Monte Carlo simulations to estimate the errors of the fitted parameters. At each data point, we generate the velocity with the Gaussian distribution defined by the intrinsic dispersion and observed velocity error. After 1000 Monte Carlo simulations, we used the 68% confidence intervals as the 1σ uncertainties of the fitted parameters.

As discussed in Strader et al. (2011), allowing the PA of the rotation axis to be a free parameter creates a tendency to overestimate the rotation amplitude. We use Monte Carlo simulations, similar to those described in Pota et al. (2013), to estimate the magnitude of this bias. The bias depends on $(V_{\mathrm{rot}}/\sigma)$, bin size and the azimuthal distribution of data points. When $(V_{\mathrm{rot}}/\sigma)$ and bin size are small, the bias will increase. Sometimes, the estimated bias is comparable to or larger than the measured v_{rot} (i.e., for VCC 685). We list the estimated bias in Table 3. However, in both cases where the bias is comparable to the rotation amplitude, the uncertainty in the rotation amplitude is also large. Thus, our conclusions are based on the rotation amplitudes without bias correction.

To compare the SAURON data, GDL, and GCs, we carry out rolling fits with the raw data binned in elliptical annuli. The
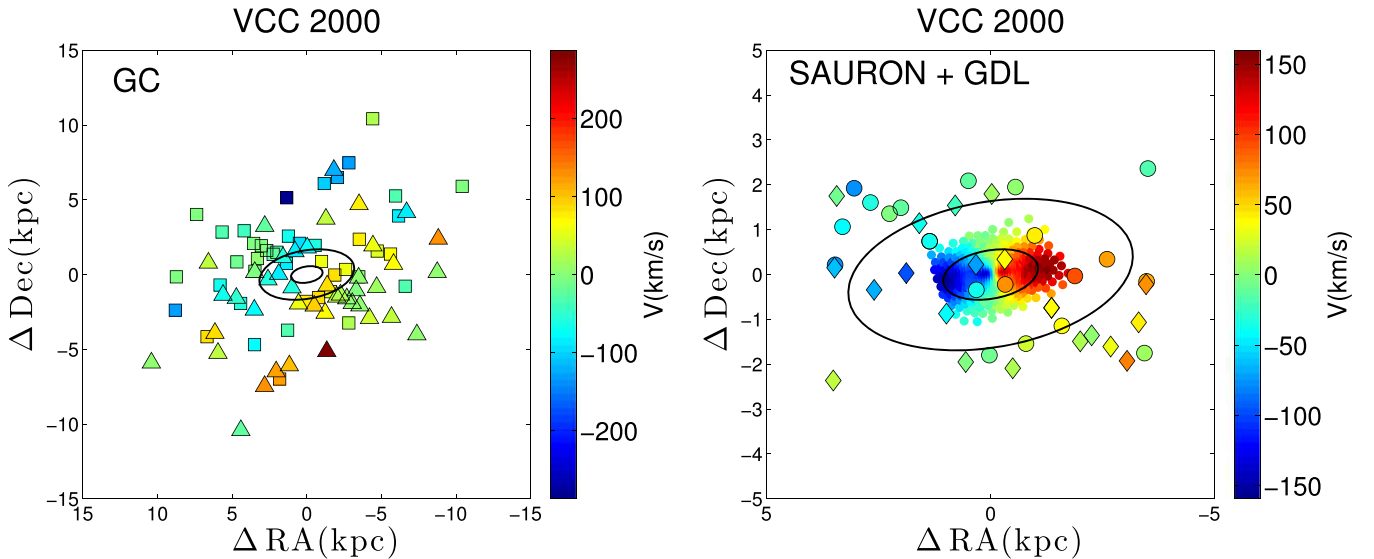

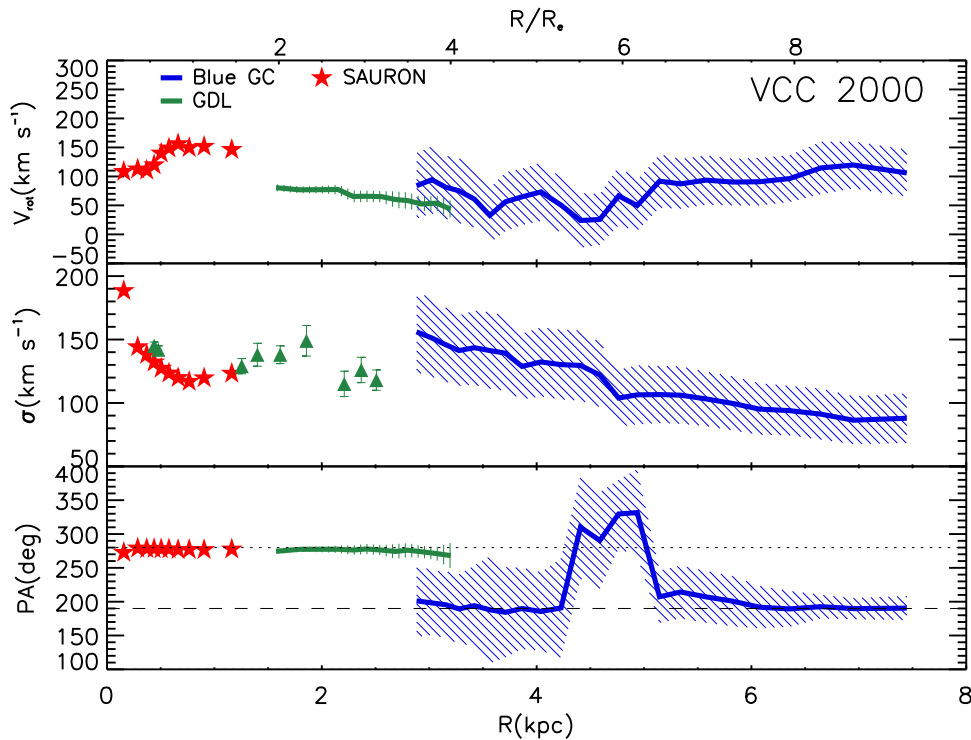**Figure 8.** Same as in Figure 5, but for VCC 2000.

Figure 9. Kinematics fitting result as a function of radius in VCC 2000. The symbols are shown in the upper left. The SAURON data and GDL show rotation around the same axis, but the GDL data (which is at larger radius) has a smaller rotation amplitude than the SAURON data. The velocity dispersion profile of the GCs decreases with radius. The PA_{kin} of the blue GCs is largely not coincident with the PA_{kin} of the GDL.
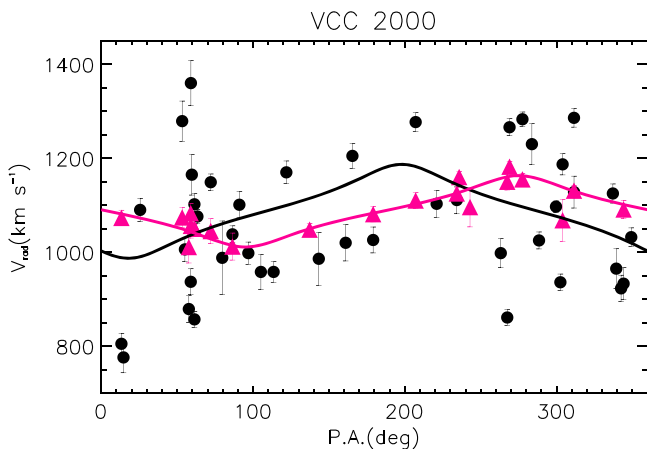

Figure 10. Radial velocities vs. position angle in VCC 2000. The GCs and the GDL both show rotation, but with different rotation axes.

number of GCs in each bin depend on the sampling of the GC system. There are 10–20 GCs and 7–10 GDL slits in one bin. We move the bins one data point at a time. The galaxy systemic velocity is fixed to the value in Table 1. The fitting results for the GC systems are listed in Tables 3–5.

4. RESULTS

4.1. VCC 1231

The 2D velocity field of VCC 1231 is shown in Figure 5. The GC and stellar velocity fields are shown in the left and right panels, respectively. The velocity field of the GCs does not show any obvious ordered motion or significant rotation.

The central stellar kinematics as shown by the SAURON data, however, show clear rotation, with a peak amplitude of $V_{rot} \sim 60 \, km \, s^{-1}$. Our GDL data goes out farther in radius than the SAURON data and is consistent with the SAURON data in the overlap region. In the outer regions, the rotation amplitude declines. Recently, Foster et al. (2013) also use a similar method to get GDL kinematics in VCC 1231, and their results show both minor and major axis rotation in the outer regions. They argue that it is tell-tale sign of triaxiality (e.g., Peng et al. 2004b). Although we do not see this kinematic structure in our GDL data, it possibly due to the fact that most of the slits where we can derive stellar kinematics are along the major axis, so it is difficult to see any major axis rotation. We also lack the data to confirm the minor axis rotation out to 5 kpc.

In Figure 6, we plot the rotation amplitude, V_{rot}, velocity dispersion, σ, and rotation axis, PA_{kin}, profiles with radius. We can see that σ and the kinematic PA of the stars in the outer regions (GDL, green solid line or triangle) is generally consistent with that measured by SAURON in the inner regions (red stars). In the region where they overlap, V_{rot} and PA_{kin} of the stars in the outer regions are a little bit offset from the SAURON data. One possibility is that our GDL kinematics are not determined from a uniform spatial distribution, which can lead to fitting bias. Moreover, the radial bin size for the SAURON profile is much smaller than for our GDL profile. The V_{rot} of GDL data is in agreement with SAURON data in 2σ confidence.

The GDL rotation amplitude is smaller than that in the inner regions. It decreases with radius and $V_{rot} \sim 20 \, km \, s^{-1}$ at 3 kpc. The PA_{kin} is $\sim 120°$ and stays the same out to 3 kpc. Similar results were also found in Foster et al. (2013, their Figure 3). We plot the GDL velocity dispersion profile in the middle
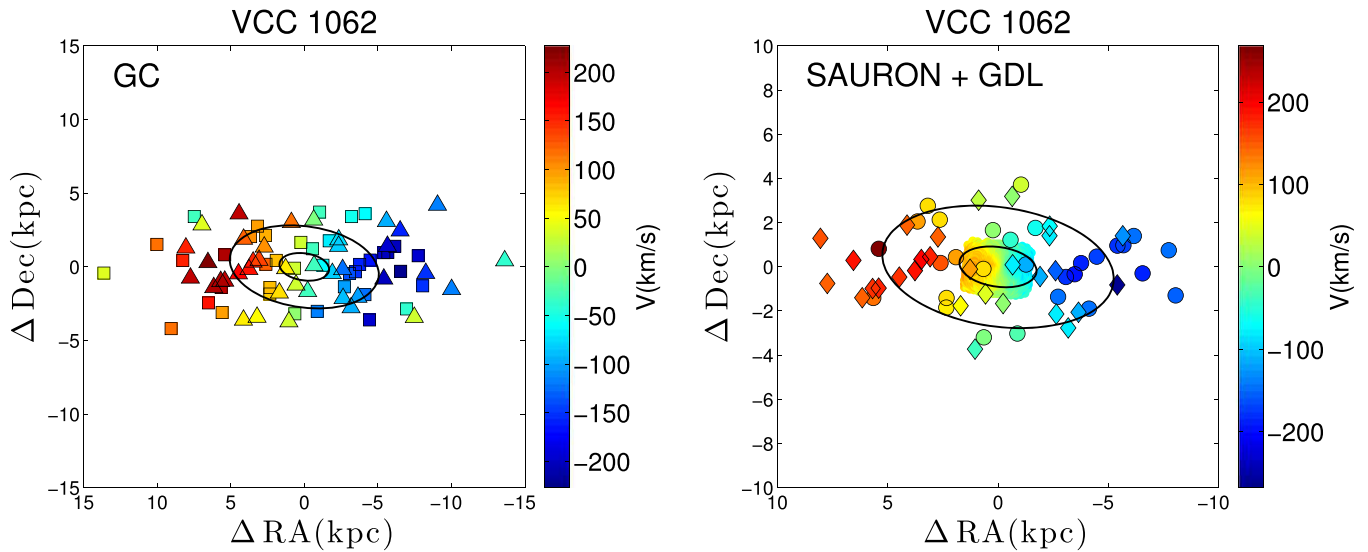
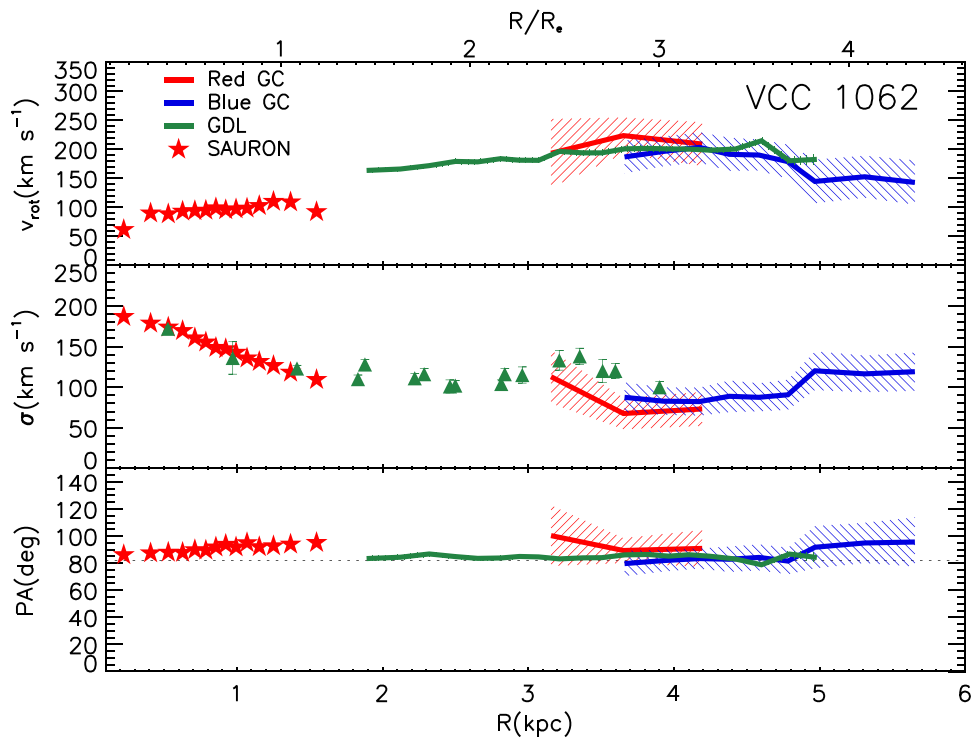**Figure 11.** Same as in Figure 5, but for VCC 1062.

Figure 12. Kinematic fitting results as a function of radius in VCC 1062. Red GCs, blue GCs, and the GDL all show significant rotation around the same rotation axis. The velocity dispersion profile of the red and blue GCs stays flat between 3 and 5 kpc, but the blue GC dispersion profile increases beyond 5 kpc.

panel of Figure 6. Each green triangle represents the measured velocity dispersion from one slit. We derived the SAURON velocity dispersion profile (red stars) by taking the mean velocity dispersion within an elliptical annulus on the 2D velocity dispersion map. These two measurements are not entirely equivalent, making GDL profile noisier than the SAURON velocity dispersion profile. However, on average, these two datas show a good agreement at the same position (see Figure 2).

The V_{rot} of red and blue GCs are similar and both nominally larger than that of the GDL, but the error is large and the low number of GCs ($10 \lesssim N \lesssim 20$) in each bin may lead to the V_{rot}

being overestimated. After the bias correction, the rotation velocity of red and blue GC is $3 \pm 115 \, \mathrm{km \, s^{-1}}$ and $52 \pm 43 \, \mathrm{km \, s^{-1}}$. The red GC rotation is consistent with zero, within the uncertainties.

Although the rotation amplitudes for the two GC subpopulations are similar, the best-fit rotation axes are very different, which is intriguing. The red GCs appear to rotate around the photometric minor axis, which is consistent with the stars in the inner regions, while the blue GCs appear to rotate around an axis somewhere between the photometric major and minor axes. These very different PAs lead to the whole GC system showing no significant rotation (see Figure 7). The best-fitting

rotation amplitude for the full GC system is 35 ± 40 km s^{-1} with PA$_{kin} = 216 \pm 78°$. To test the significance of this rotation signal, we use the method of "scrambling" the properties of the observed GCs and refitting the kinematics. This method had been applied in testing the rotation of the M87 UCD system (Zhang et al. 2015) and the GC systems of low-mass galaxies (Toloba et al. 2015b). We fix the GC PAs and randomly shuffle the velocity and velocity error of each GC. We repeated this exercise 1000 times and each time we apply the same kinematics fitting as we did for our original data. We find that 88% and 33% of the simulations for the red and blue GCs, respectively, have rotation amplitudes at least as high as what we fit for our observed data. We conclude that the significance of these rotation amplitudes is not high, but future observations to obtain more GC velocities may shed further light on this issue.

In Figure 7, we also plot the GDL best-fitting rotation curve. The GDL best-fitting amplitude is 41 ± 6 km s^{-1} with PA$_{kin} = 129 \pm 7°$, which is smaller than the SAURON data in the inner region.
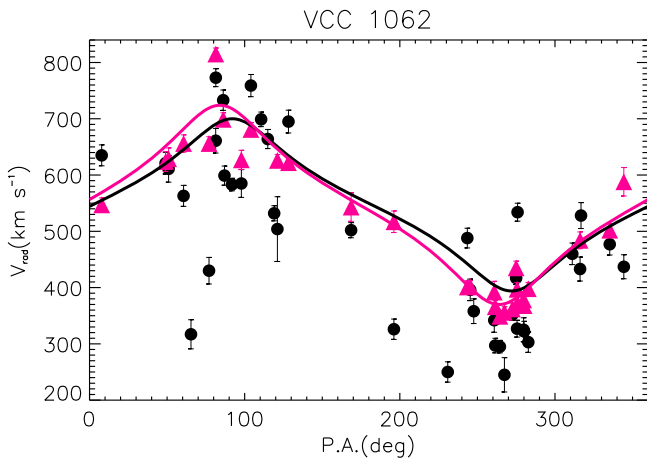
4.2. VCC 2000

The right panel of Figure 8 shows the 2D velocity field of stars in VCC 2000. Both the SAURON and GMOS data show obvious rotation with the same PA$_{kin}$, although the rotation velocity in the inner regions seems larger than in the outer regions. The GCs show rotation in the inner region $\lesssim 3R_e$ and outer region. In the middle region, however, the rotation velocity dips to ~40 km s^{-1}. There are 42 blue GCs and only 1 red GC in VCC 2000, so we only plot the blue GCs in Figure 9.

Although there is little overlap between the SAURON and GMOS data for the stars, the stellar rotation axis (PA$_{kin}$) is consistent across both data sets, with both showing rotation about the photometric minor axis. However, the amplitude of the rotation appears to decline with radius. The rotation amplitude of the GC system is consistent with that of the stars in their region of overlap, but the axis of rotation is off by 90°, with the GCs rotating about the photometric major axis. The GCs and the stars appear kinematically decoupled in this galaxy. The velocity dispersion of the GCs monotonically declines.

The best fitting PA versus V_{rad} curve is shown in Figure 10. The GC best-fitting amplitude is 100 ± 42 km s^{-1} with PA$_{kin} = 198 \pm 32°$. The GDL best-fitting amplitude is 76 ± 6 km s^{-1} with PA$_{kin} = 275 \pm 4°$. This again shows that the GCs and stars both show rotation, but with the different PAs for their rotation axes. The rotation velocity of the GDL is smaller than that derived from the SAURON data in the inner regions.

4.3. VCC 1062

The 2D velocity fields of VCC 1062 are shown in Figure 11. In this galaxy, both the stars and GCs show strong rotation about the minor axis at all radii. The blue and red GCs also exhibit similar kinematics. In Figure 12, we can see that the rotation amplitude of the stars and GCs at large radii ($R > 2$ kpc) stays flat at around 200 km s^{-1}. The GCs also have a rotation axis similar to that fit to the stellar SAURON data in the inner region.

The best fitting rotation curve of VCC 1062 is shown in Figure 13. We can see that the stars (GDL) and GC both show
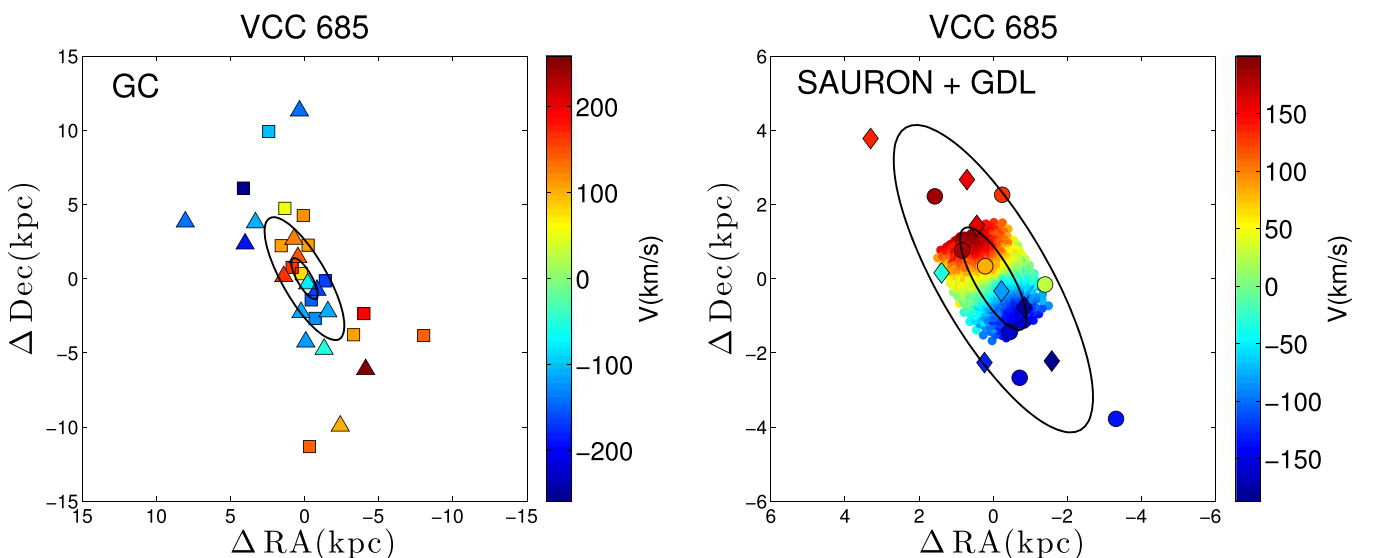

Figure 13. Radial velocities vs. position angle in VCC 1062. The GCs and GDL both show significant rotation about the same axis.

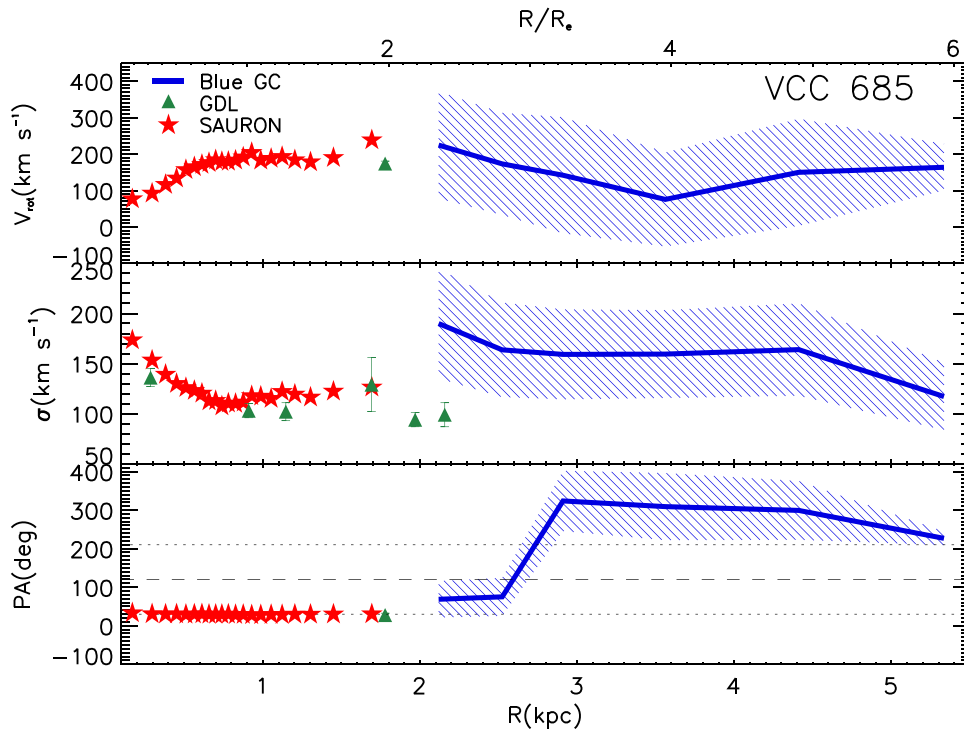**Figure 14.** Same as in Figure 5, but for VCC 685.

Figure 15. Kinematics fitting result as a function of radius in VCC 685. The blue GCs exhibit counter-rotation, showing rotation in both the inner and outer regions, but around different rotation axes. The velocity dispersion profile of GC stays flat with radius.
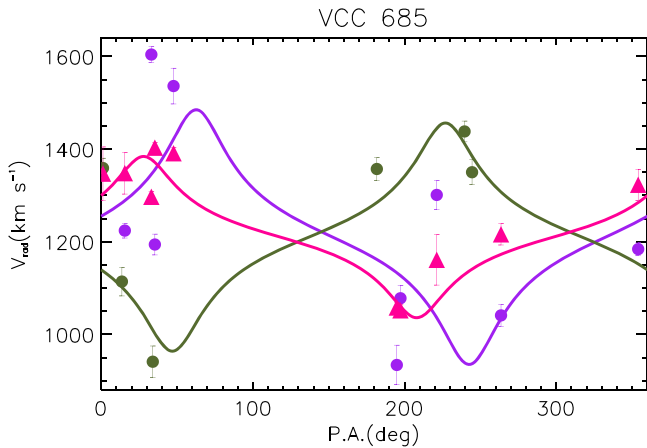

Figure 16. Radial velocities vs. position angle in VCC 685. The purple and green circles represent the inner and outer region GCs, respectively. The fits show strong counter-rotation. The magenta curve and points represents the rotation of the GDL, which lines up more with the rotation of the inner GCs.

a significant rotation with the same PA_{kin}. The GCs best-fitting amplitude is 153 ± 28 km s^{-1} with $PA_{kin} = 92 \pm 12°$. The GDL best-fitting amplitude is 177 ± 3 km s^{-1} with $PA_{kin} = 84 \pm 1°$. The peak rotation is essentially along the photometric major axis (i.e., rotating about the minor axis). The rotation velocity of the GDL is larger than that for the SAURON data in the inner region.

4.4. VCC 685

VCC 685 is also classified as a fast rotator in the ATLAS^{3D} project. The stars clearly rotate about the photometric minor axis (Krajnović et al. 2011). Our GMOS GDL measurements are consistent with the SAURON data, and we can clearly see rotation in the 2D velocity field of the stars out to $3R_e$ (Figure 14, right panel, Figure 15, top panel). In these inner regions, the GCs also show strong rotation about the photometric minor axis, but there is a remarkable shift at $R = 3$–4 kpc. At these radii, the rotation axis of the GCs flips and exhibits counter-rotation. To better quantify this, we divide the GCs into two groups: 9 GCs in the inner region (<3.5 kpc) and 6 GCs in the outer region (>3.5 kpc). The best-fitting rotation curve for the inner and outer GC samples are shown in Figure 16. The purple and green circles represent the inner and outer region GCs, respectively. The inner region GCs' best-fitting amplitude is 282 ± 129 km s^{-1} with $PA_{kin} = 64 \pm 38°$. The outer region GCs best-fitting amplitude is 245 ± 85 km s^{-1} with $PA_{kin} = 224 \pm 13°$.

Given that we only have 15 GCs in this galaxy, we wanted to see if this situation could occur randomly. To test the significance of the counter rotation, we used the scrambling method discussed earlier where we fix the PAs of the GCs and randomly scramble the velocities and velocity errors. After 100,000 trials, we find that only 520 have kinematics similar to what we observe ($V_{rot,inner} \geqslant 282$, $V_{rot,outer} \geqslant 245$, and $121° < \Delta PA_{kin} < 239°$). With only 0.52% of trials randomly producing the observed kinematics, we conclude that this detection of counter-rotation in the GCs is significant.

In Figure 16, we show that the best-fitting amplitude of GDL is 174 ± 7 km s^{-1} with the PA_{kin} is $28 \pm 5°$. This is consistent with the results from fitting the SAURON data. These stellar kinematics are roughly (but not exactly) consistent with the kinematics of the inner GCs.

Table 5
Bright and Faint GC Kinematics Fitting Results

ID	$V_{rot,b}$ (km s^{-1})	$V_{rot,f}$ (km s^{-1})	Bias$_b$ (km s^{-1})	Bias$_f$ (km s^{-1})	σ_b (km s^{-1})	σ_f (km s^{-1})	PA$_{kin,b}$ (degree)	PA$_{kin,f}$ (degree)	g (magnitude)
(1)	(2)	(3)	(4)	(5)	(6)	(7)	(8)	(9)	(10)
VCC1231	118 ± 62	28 ± 56	17	54	171 ± 31	162 ± 30	224 ± 45	94 ± 98	22.274
VCC2000	119 ± 64	99 ± 46	20	16	138 ± 31	119 ± 27	204 ± 45	182 ± 31	22.250
VCC1062	139 ± 29	170 ± 50	8	13	77 ± 17	134 ± 28	88 ± 16	94 ± 20	22.458

Note. Column (2–9): Bright (*b*) and faint (*f*) GC kinematics results for our galaxy sample. Column (10): The divided *g*-band magnitude for the bright and faint group.
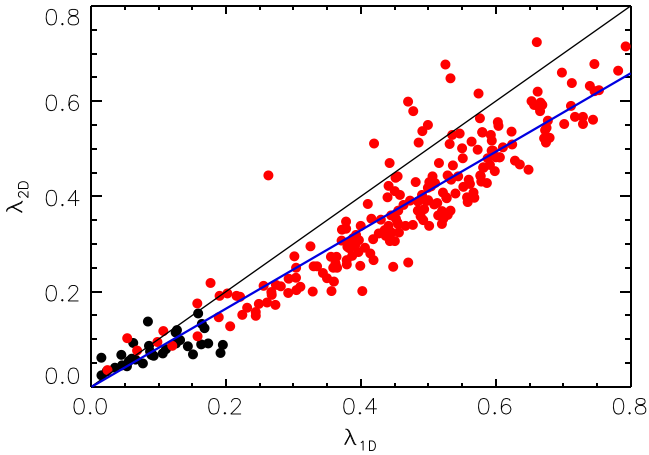

Figure 17. Comparison of λ_{1D} and λ_{2D}. The black points and the red points represent the slow and fast rotator. The black line is a 1:1 relation. The blue line show the best fitting linear relation to the data.

5. DISCUSSION

5.1. The Kinematics of GC Systems and Their Hosts

The four galaxies in our sample are similar in many respects. All are classified as "fast rotators" by the ATLAS[3D] project, have similar morphological classifications, have nearly identical surface brightness profiles (Sersić $n \sim 3$–4) and GC surface density profile shapes (Sérsic $n \sim 1.2$–1.8). Yet, their GC systems show different kinematics: VCC 1231's GCs show little or no rotation. VCC 2000 GCs have a rotation amplitude consistent with the stars, but with a different rotation axis (PA$_{kin}$). VCC 1062's GCs show fast rotation consistent with the stars both in amplitude and PA. VCC 685's GC system exhibits counter-rotation. This diversity suggests that these galaxies, despite their otherwise similar characteristics, had different assembly histories. Below, we discuss each of the galaxies in more detail.

1. *VCC 1231*: Although the GC system as a whole does not show significant rotation, the red and blue GC individually appear to have rotation around nearly opposite kinematic axes, and with the red GCs aligned with the rotation of the stars. This finding is currently of low significance due to the low number of GCs in each sample. Many observations suggest that the red GCs are more associated with the stellar main body (Peng et al. 2004a; Faifer et al. 2011; Strader et al. 2011; Pota et al. 2013). It will be interesting to observe more GCs to test if the metal-poor GCs are truly counter-rotating with respect to the metal-rich GCs and the stars. If true, and if the metal-poor GCs are accreted from low-mass

progenitors (e.g., Cote et al. 1998), then this galaxy requires a formation scenario where the angular momenta of the dry merged components and the gaseous components are nearly opposite.

2. *VCC 2000*: This galaxy's GC system is a more significant example of where the kinematics of blue GCs are different from those of the stars (see Figure 10). In this case the rotation axis of the blue GCs is orthogonal to that of the stars. This galaxy GC system is consistent with a scenario where blue GCs are accreted from low-mass progenitor, and where the kinematics of these outer components are decoupled from the material that eventually settles to form the stellar disk.

3. *VCC 1062*: This galaxy's kinematics are the "simplest" in our sample. The red and blue GCs both have kinematics consistent with the stars. All three components of this galaxy show fast rotation about a common axis, the minor axis. In this case, the angular momenta of the progenitors that formed these components were all aligned.

4. *VCC 685*: The kinematics of the GCs in VCC 685 are the most complex and tantalizing. Kinematically decoupled cores, or kinematically distinct components (KDCs), have been found in the stellar kinematics in the central regions of many galaxies. This designation refers to an abrupt kinematic change between then the inner and outer regions of a galaxy (Rix et al. 1992; Mehlert et al. 1998; Wernli et al. 2002; Krajnović et al. 2011; Arnold et al. 2014; Toloba et al. 2014). In VCC 685, we find evidence that the GCs in the inner and outer regions are counter-rotating with respect to one another, with the inner component roughly aligned with the stars. This suggests discrete merging events. Indeed, for stellar KDCs, gas-rich mergers are often invoked as an explanation. In this case, however, the kinematic transition happens at much larger radii than for the stellar KDCs that are traditionally discussed (although Arnold et al. 2014 find evidence of this behavior in some of their sample galaxies). More GC data, more stellar kinematic data at larger radii, and realistic simulations are needed to investigate the counter-rotation in this galaxy.

Lastly, we also analyze the kinematics of GCs subdivided by GC luminosity. Table 5 shows the rotation and velocity dispersion fitting results for subsamples of bright and faint GCs. We choose to divide the GC sample at the magnitude at which we have equal numbers of GCs in the two subsamples. The divided magnitude is shown in the last column of Table 5. For VCC 1231, we find that the brighter GCs have significantly more rotation than the fainter ones, which are consistent with no rotation. This is possibly because the brightest GCs are more likely to be blue, and hence their kinematics mirror the blue GCs. The fainter sample contains both blue and red GCs, and

Table 6
General Properties of Literature Galaxies

ID	R_e (kpc)	M_K (mag)	D (Mpc)	ϵ_{star}	N_{GC}	$\lambda_{1D,GC,\epsilon=0}$	$\lambda_{1D,GC,\epsilon=star}$	Rotation $<1R_e$	References
(1)	(2)	(3)	(4)	(5)	(6)	(7)	(8)	(9)	(10)
NGC 4494	4.3	−24.2	16.6	0.13	117	0.46 ± 0.04	0.48 ± 0.04	F	F + 11
NGC 3379	2.0	−23.7	10.2	0.15	52	0.10 ± 0.03	0.13 ± 0.03	F	P + 04; P + 06; B + 06
NGC 4636	6.1	−24.3	14.2	0.16	459	0.21 ± 0.02	0.22 ± 0.02	S	S + 12
NGC 4472 (VCC 1226, M49)	7.7	−25.6	16.7	0.19	263	0.17 ± 0.04	0.22 ± 0.05	S	C + 03
NGC 4649 (VCC 1978, M60)	7.7	−25.3	16.3	0.19	121	0.53 ± 0.02	0.56 ± 0.02	F	H + 08
NGC 4486 (VCC 1316, M87)	13.1	−25.3	16.5	0.14	1004	0.20 ± 0.01	0.19 ± 0.01	S	S + 11; Z + 15[a]

Note. The effective radii (2) are from Ferrarese et al. (2006) and Emsellem et al. (2011). The K-band absolute magnitude (3) and distance (4) are from Pota et al. (2013), Tables 1 and 7, where (3) is derived from 2MASS apparent magnitude and (4) are from Tonry et al. (2001) and Mei et al. (2007). (5) is the ellipticity with $1 - (b/a)_k$, where the axis ratio are from 2MASS. (6) is the total number of GCs with measured radial velocities. (7) and (8) are the projected specific angular momentum with $\epsilon = 0$ and $\epsilon = \epsilon_{star}$. (9) Whether a galaxy is classified as a fast or slow rotator in ATLAS^{3D} (Emsellem et al. 2011). (10) References: F + 11(Foster et al. 2011) ; P + 04(Puzia et al. 2004); P + 06 (Pierce et al. 2006); B + 06(Bergond et al. 2006); S + 12(Schuberth et al. 2012); C + 03(Côté et al. 2003); H + 08 (Hwang et al. 2008); S + 11(Strader et al. 2011); Z + 15(Zhang et al. 2015).
[a] New GC data from our MMT observations, described by Zhang et al. (2015), are combined with previously published data.

Table 7
Specific Angular Momentum

ID	λ_{2D} (SAURON)	λ_{1D} (SAURON)	λ_{1D} (GDL)	$\lambda_{1D,GC,\epsilon=0}$ (GCs)	$\lambda_{1D,GC,\epsilon=star}$ (GCs)
(1)	(2)	(3)	(4)	(5)	(6)
VCC1231	0.23	0.34	0.17 ± 0.02	0.04 ± 0.04	0.08 ± 0.06
VCC2000	0.55	0.70	0.49 ± 0.02	0.30 ± 0.06	0.32 ± 0.06
VCC1062	0.36	0.51	0.84 ± 0.01	0.82 ± 0.03	0.88 ± 0.02

Note. (2) λ_{2D} measurement from SAURON data, (3) λ_{1D} measurement from SAURON data, (4) λ_{1D} measurement from Gemini (GDL), (5) and (6) $\lambda_{1D,GC}$ for the GCs assuming different ellipticities. The uncertainties for the SAURON data are very small, and they are not listed in the table.
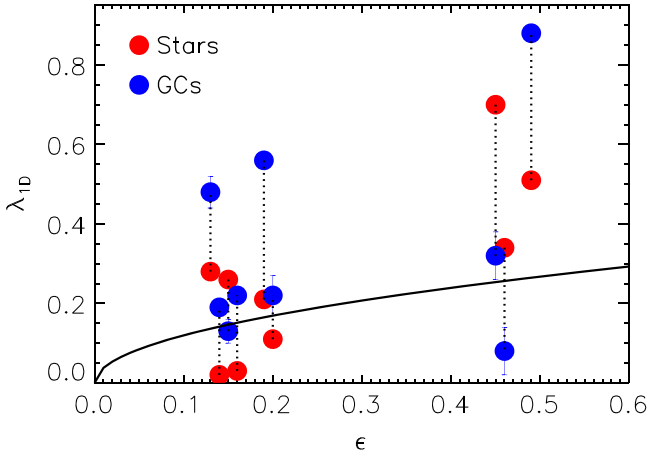
Figure 18. Specific angular momentum of GCs and SAURON data as function of ellipticity. The red circles represent the λ_{1D} of the GC. The blue circles represent the λ_{1D} of the SAURON data. The dash lines link the same galaxy. The solid line is $\lambda_{1D} = 0.38 \times \sqrt{\epsilon}$. Most stellar slow rotators also show slow rotation in their GC systems, with $\lambda_{GC} \sim 0.2$. Stellar fast rotators display a large range in λ_{GC}.

Figure 19. λ_{1D} and the ellipticity profiles as radius for VCC 1231, 2000, and 1062. In the top panel, the solid curve represents the λ_{1D} profile measurements from SAURON data. The dash curve represents the λ_{1D} profile measurement from the GDL. The individual λ_{1D} profiles (SAURON and GDL) are each cumulative with radius, but the two data sets are treated separately to allow for a comparison.

so their kinematics are a combination of these apparently counter-rotating populations. The other two galaxies do not show very significant differences in the rotation properties between the bright and faint GCs. VCC 1062's bright GCs, however, have a noticeably lower velocity dispersion $(77 \pm 17\,\mathrm{km\,s^{-1}})$ compared to their fainter counterparts $(134 \pm 28\,\mathrm{km\,s^{-1}})$. These differences are worth further exploration in the future with larger data sets.

5.2. Specific Angular Momentum

To provide a more quantitative look at the kinematics of ETGs, we use the specific angular momentum. An early study of the M87 GC system used a dimensionless spin parameter (Kissler-Patig & Gebhardt 1998). We use the dimensionless

Figure 20. 2D velocity and velocity dispersion fiedls of VCC 1231 and 2000, without smooth and double data.

Figure 21. Same as in Figure 20, but for VCC 1062 and 685.

Table 8
Globular Cluster

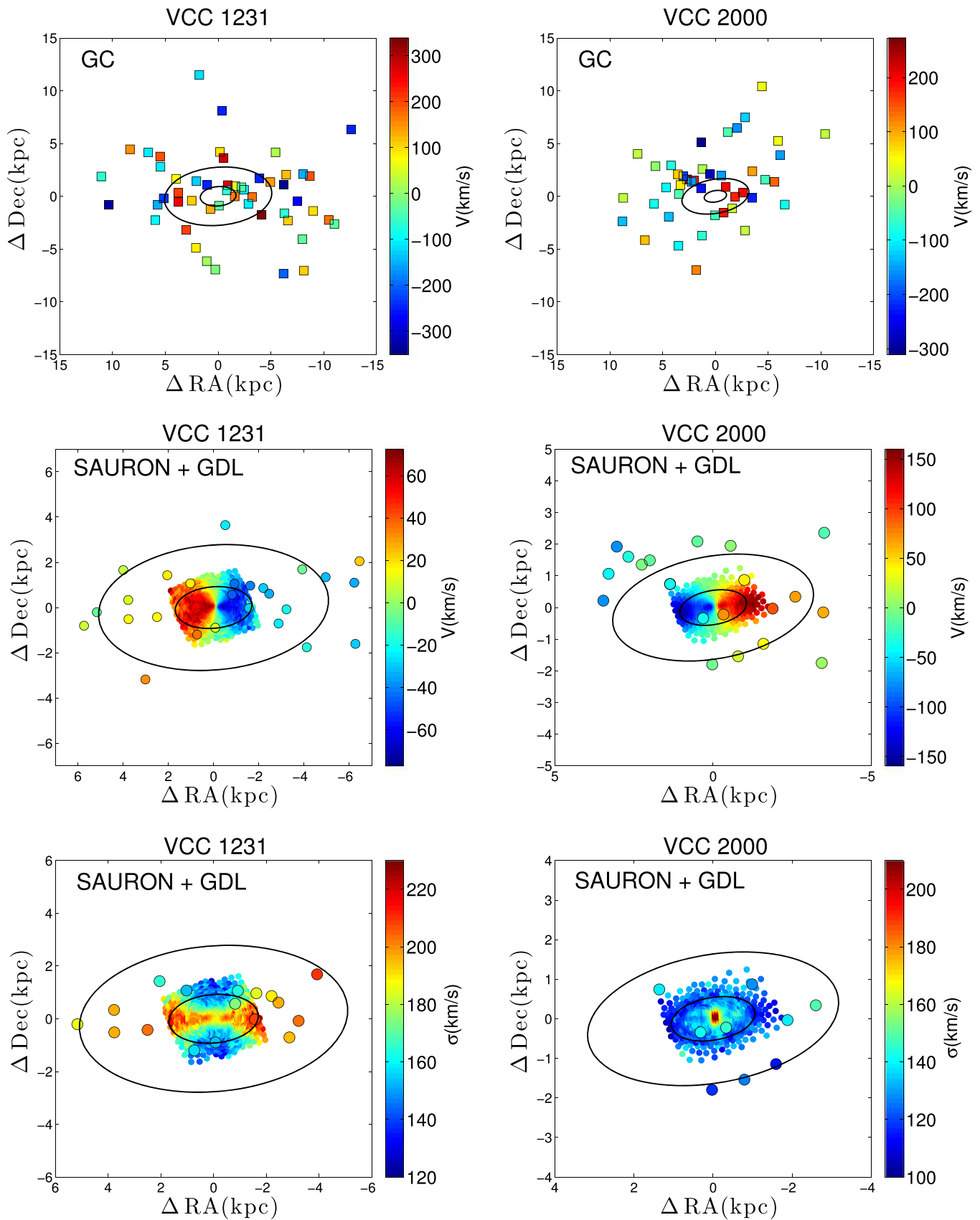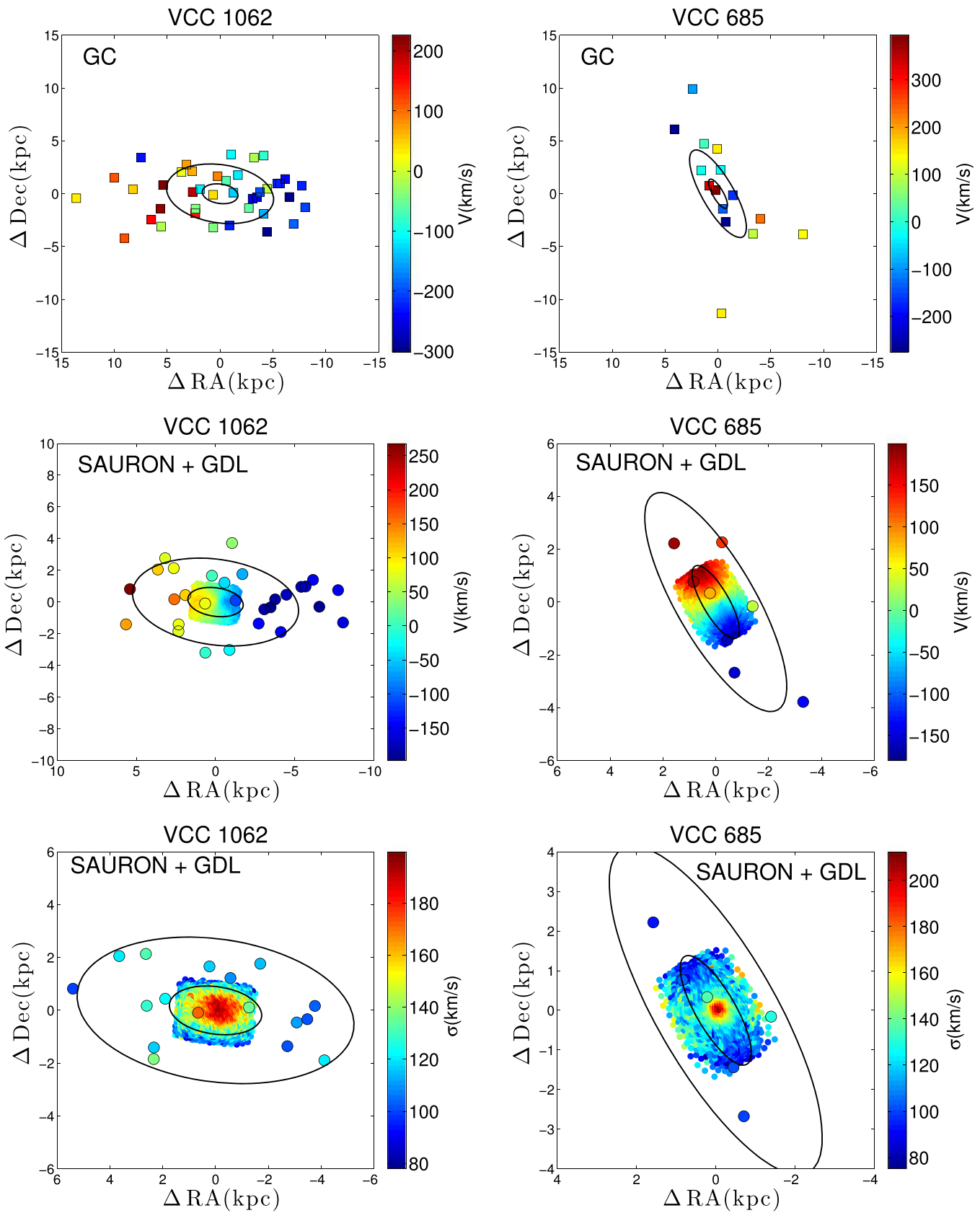| ID	R.A.(J2000)	Decl.(J2000)	$v_{\rm los}$	g	z	$g - z$	$E(B - V)$
	(deg)	(deg)	(km s^{-1})	(mag)	(mag)	(mag)	(mag)
(1)	(2)	(3)	(4)	(5)	(6)	(7)	(8)
VCC 1231							
VCC1231GC-01	187.420170	13.436530	2450 ± 19	21.280 ± 0.016	20.229 ± 0.024	0.991 ± 0.007	0.028
VCC1231GC-02	187.422675	13.437170	2107 ± 22	21.960 ± 0.026	20.922 ± 0.029	0.973 ± 0.033	0.028
VCC1231GC-03	187.428810	13.436997	2377 ± 20	22.192 ± 0.022	20.893 ± 0.020	1.253 ± 0.028	0.028
VCC1231GC-04	187.413315	13.420913	2429 ± 15	22.233 ± 0.030	20.788 ± 0.019	1.374 ± 0.024	0.028
VCC1231GC-05	187.418970	13.424147	2357 ± 17	23.033 ± 0.032	22.196 ± 0.031	0.817 ± 0.022	0.028
VCC1231GC-06	187.411215	13.419499	2229 ± 21	23.147 ± 0.038	22.185 ± 0.031	0.907 ± 0.025	0.028
VCC1231GC-07	187.405065	13.453014	2007 ± 18	22.096 ± 0.007	21.359 ± 0.016	0.703 ± 0.012	0.028
VCC1231GC-08	187.429815	13.401846	2058 ± 49	22.933 ± 0.013	22.271 ± 0.037	0.551 ± 0.030	0.028
VCC1231GC-09	187.432710	13.444921	2282 ± 20	22.855 ± 0.022	21.790 ± 0.021	1.018 ± 0.025	0.028
VCC1231GC-10	187.441245	13.429025	2435 ± 28	21.842 ± 0.037	20.977 ± 0.018	0.799 ± 0.039	0.028
VCC1231GC-11	187.437780	13.422738	2599 ± 24	21.821 ± 0.012	20.903 ± 0.020	0.832 ± 0.019	0.028
VCC1231GC-12	187.447410	13.432945	2324 ± 20	21.209 ± 0.029	20.154 ± 0.020	0.992 ± 0.028	0.028
VCC1231GC-13	187.450110	13.433290	2533 ± 21	21.813 ± 0.019	20.817 ± 0.012	0.946 ± 0.020	0.028
VCC1231GC-14	187.454700	13.403273	2250 ± 24	22.485 ± 0.018	21.570 ± 0.016	0.871 ± 0.022	0.028
VCC1231GC-15	187.452990	13.445077	2356 ± 20	21.861 ± 0.017	20.343 ± 0.013	1.436 ± 0.016	0.028
VCC1231GC-16	187.456470	13.424834	2389 ± 27	22.005 ± 0.020	20.962 ± 0.015	0.990 ± 0.021	0.028
VCC1231GC-17	187.463295	13.427741	2367 ± 17	21.306 ± 0.014	20.320 ± 0.017	0.920 ± 0.019	0.028
VCC1231GC-18	187.474695	13.439762	2151 ± 26	22.359 ± 0.022	21.412 ± 0.016	0.885 ± 0.022	0.028
VCC1231GC-19	187.468155	13.427391	2523 ± 17	21.806 ± 0.032	20.469 ± 0.011	1.274 ± 0.028	0.028
VCC1231GC-20	187.475715	13.426306	2107 ± 29	22.550 ± 0.020	21.521 ± 0.019	0.967 ± 0.022	0.028
VCC1231GC-21	187.469025	13.435520	2337 ± 20	22.932 ± 0.025	21.607 ± 0.014	1.278 ± 0.024	0.028
VCC1231GC-22	187.479150	13.444892	2148 ± 23	22.673 ± 0.023	21.639 ± 0.015	1.014 ± 0.026	0.028
VCC1231GC-23	187.485810	13.446020	2412 ± 15	21.166 ± 0.032	20.194 ± 0.022	0.880 ± 0.022	0.028
VCC1231GC-24	187.496295	13.436360	2200 ± 11	21.183 ± 0.004	20.467 ± 0.008	0.647 ± 0.007	0.028
VCC1231GC-25	187.429695	13.433433	1909 ± 15	22.667 ± 0.017	21.218 ± 0.019	1.384 ± 0.019	0.028
VCC1231GC-26	187.424715	13.427611	1988 ± 23	22.616 ± 0.017	21.261 ± 0.018	1.294 ± 0.019	0.028
VCC1231GC-27	187.422900	13.414083	2226 ± 26	22.785 ± 0.056	21.737 ± 0.062	0.909 ± 0.021	0.028
VCC1231GC-28	187.422360	13.402969	2364 ± 14	21.274 ± 0.003	20.445 ± 0.007	0.763 ± 0.006	0.028
VCC1231GC-29	187.450515	13.431453	2198 ± 31	21.206 ± 0.014	20.287 ± 0.018	0.849 ± 0.014	0.028
VCC1231GC-30	187.447620	13.429241	2418 ± 23	21.843 ± 0.025	20.514 ± 0.016	1.262 ± 0.027	0.028
VCC1231GC-31	187.442595	13.426672	2151 ± 20	21.411 ± 0.016	20.467 ± 0.013	0.876 ± 0.015	0.028
VCC1231GC-32	187.461765	13.411035	2351 ± 16	22.139 ± 0.080	21.053 ± 0.022	0.999 ± 0.074	0.028
VCC1231GC-33	187.434585	13.434356	2397 ± 16	22.953 ± 0.027	21.884 ± 0.025	0.990 ± 0.025	0.028
VCC1231GC-34	187.444185	13.431620	2155 ± 69	22.671 ± 0.023	21.758 ± 0.023	0.826 ± 0.023	0.028
VCC1231GC-35	187.457610	13.433330	2013 ± 24	22.274 ± 0.020	21.276 ± 0.020	0.931 ± 0.023	0.028
VCC1231GC-36	187.452285	13.459685	2012 ± 38	22.952 ± 0.034	21.852 ± 0.026	1.031 ± 0.031	0.028
VCC1231GC-37	187.460490	13.472438	2140 ± 21	21.361 ± 0.005	20.300 ± 0.007	1.046 ± 0.006	0.028
VCC1231GC-38	187.473540	13.428547	2033 ± 35	22.964 ± 0.053	22.082 ± 0.042	0.821 ± 0.064	0.028
VCC1231GC-39	187.493505	13.426348	1929 ± 34	20.809 ± 0.002	19.955 ± 0.005	0.755 ± 0.005	0.028
VCC1231GC-40	187.428210	13.420699	2371 ± 32	23.131 ± 0.017	21.801 ± 0.012	1.271 ± 0.019	0.028
VCC1231GC-41	187.429515	13.423301	2199 ± 48	23.347 ± 0.025	22.404 ± 0.022	0.885 ± 0.029	0.028
VCC1231GC-42	187.451670	13.442974	2538 ± 16	22.347 ± 0.016	21.181 ± 0.025	1.114 ± 0.029	0.028
VCC1231GC-43	187.457820	13.406286	2272 ± 15	21.564 ± 0.016	20.385 ± 0.018	1.075 ± 0.014	0.028
VCC1231GC-44	187.465260	13.417413	2467 ± 11	20.955 ± 0.024	19.776 ± 0.012	1.126 ± 0.023	0.028
VCC1231GC-45	187.453365	13.425970	2230 ± 14	21.304 ± 0.021	20.272 ± 0.015	0.957 ± 0.017	0.028
VCC1231GC-46	187.438560	13.435633	2014 ± 17	22.761 ± 0.015	21.614 ± 0.020	1.070 ± 0.020	0.028
VCC1231GC-47	187.445190	13.432550	2213 ± 36	23.151 ± 0.026	21.727 ± 0.022	1.358 ± 0.031	0.028
VCC1231GC-48	187.461540	13.434665	2125 ± 27	22.784 ± 0.024	21.886 ± 0.016	0.837 ± 0.026	0.028
VCC1231GC-49	187.474830	13.443451	2450 ± 20	22.730 ± 0.021	21.425 ± 0.020	1.236 ± 0.026	0.028
VCC1231GC-50	187.468185	13.430573	2459 ± 38	23.187 ± 0.015	21.905 ± 0.026	1.206 ± 0.021	0.028
VCC1231GC-51	187.476593	13.420838	2161 ± 24	22.740 ± 0.012	21.886 ± 0.028	0.678 ± 0.021	0.028
VCC 2000							
VCC2000GC-01	191.092740	11.213082	1081 ± 12	20.572 ± 0.002	19.893 ± 0.005	0.611 ± 0.004	0.034
VCC2000GC-02	191.122215	11.219080	949 ± 42	22.741 ± 0.027	21.912 ± 0.027	0.778 ± 0.025	0.034
VCC2000GC-03	191.125230	11.215344	907 ± 28	22.478 ± 0.029	21.556 ± 0.029	0.906 ± 0.022	0.034
VCC2000GC-04	191.128680	11.213797	1016 ± 19	22.727 ± 0.066	21.802 ± 0.052	0.889 ± 0.028	0.034
VCC2000GC-05	191.109285	11.205482	920 ± 17	21.151 ± 0.015	20.243 ± 0.014	0.889 ± 0.022	0.034
VCC2000GC-06	191.138010	11.200358	1074 ± 24	22.548 ± 0.069	21.258 ± 0.023	1.181 ± 0.070	0.034
VCC2000GC-07	191.135130	11.198518	789 ± 22	21.885 ± 0.032	20.882 ± 0.063	0.863 ± 0.032	0.034

Table 8
(Continued)

ID	R.A.(J2000)	Decl.(J2000)	v_{los}	g	z	$g - z$	$E(B - V)$
	(deg)	(deg)	(km s^{-1})	(mag)	(mag)	(mag)	(mag)
(1)	(2)	(3)	(4)	(5)	(6)	(7)	(8)
VCC2000GC-08	191.131050	11.197987	917 ± 33	22.523 ± 0.032	21.546 ± 0.013	0.895 ± 0.035	0.034
VCC2000GC-09	191.114865	11.196526	1009 ± 18	22.778 ± 0.027	21.642 ± 0.014	1.071 ± 0.028	0.034
VCC2000GC-10	191.149545	11.201708	990 ± 25	22.250 ± 0.023	21.305 ± 0.020	0.888 ± 0.025	0.034
VCC2000GC-11	191.143635	11.196664	1344 ± 48	22.456 ± 0.036	21.622 ± 0.029	0.760 ± 0.031	0.034
VCC2000GC-12	191.140995	11.196223	1263 ± 42	22.247 ± 0.019	21.427 ± 0.014	0.752 ± 0.020	0.034
VCC2000GC-13	191.146065	11.194601	1133 ± 17	22.156 ± 0.019	20.993 ± 0.015	1.116 ± 0.021	0.034
VCC2000GC-14	191.151405	11.193774	972 ± 78	22.561 ± 0.020	21.807 ± 0.013	0.705 ± 0.022	0.034
VCC2000GC-15	191.167200	11.189954	1085 ± 28	21.389 ± 0.004	20.758 ± 0.011	0.576 ± 0.007	0.034
VCC2000GC-16	191.119545	11.199561	1171 ± 22	22.462 ± 0.017	21.455 ± 0.015	0.959 ± 0.019	0.034
VCC2000GC-17	191.125890	11.190406	1250 ± 18	22.211 ± 0.033	20.846 ± 0.015	1.279 ± 0.025	0.034
VCC2000GC-18	191.107575	11.187544	982 ± 31	22.356 ± 0.015	21.531 ± 0.021	0.742 ± 0.021	0.034
VCC2000GC-19	191.123100	11.191837	1267 ± 15	21.029 ± 0.024	20.032 ± 0.022	0.907 ± 0.021	0.034
VCC2000GC-20	191.129370	11.193860	1270 ± 19	21.611 ± 0.027	20.632 ± 0.019	0.903 ± 0.011	0.034
VCC2000GC-21	191.111385	11.195764	1214 ± 43	23.032 ± 0.029	22.234 ± 0.030	0.719 ± 0.034	0.034
VCC2000GC-22	191.141985	11.195713	921 ± 27	22.467 ± 0.032	21.466 ± 0.018	0.942 ± 0.033	0.034
VCC2000GC-23	191.138505	11.193366	841 ± 17	21.266 ± 0.019	20.263 ± 0.013	0.933 ± 0.017	0.034
VCC2000GC-24	191.146710	11.191358	1022 ± 18	20.553 ± 0.058	19.691 ± 0.052	0.787 ± 0.023	0.034
VCC2000GC-25	191.155815	11.187847	982 ± 23	21.848 ± 0.029	20.955 ± 0.023	0.870 ± 0.031	0.034
VCC2000GC-26	191.150445	11.183163	942 ± 21	21.543 ± 0.031	20.743 ± 0.034	0.731 ± 0.011	0.034
VCC2000GC-27	191.145060	11.197882	863 ± 28	22.877 ± 0.024	22.085 ± 0.020	0.729 ± 0.026	0.034
VCC2000GC-28	191.159205	11.174632	1154 ± 24	21.152 ± 0.003	20.439 ± 0.008	0.635 ± 0.006	0.034
VCC2000GC-29	191.138430	11.210131	760 ± 32	22.579 ± 0.030	21.743 ± 0.021	0.768 ± 0.026	0.034
VCC2000GC-30	191.127015	11.186158	1095 ± 29	22.510 ± 0.032	21.358 ± 0.017	1.079 ± 0.024	0.034
VCC2000GC-31	191.119665	11.189951	845 ± 16	20.777 ± 0.022	19.771 ± 0.019	0.937 ± 0.022	0.034
VCC2000GC-32	191.130135	11.184649	1261 ± 19	21.572 ± 0.020	20.567 ± 0.008	0.900 ± 0.019	0.034
VCC2000GC-33	191.133315	11.183667	1010 ± 27	22.594 ± 0.032	21.563 ± 0.024	0.970 ± 0.036	0.034
VCC2000GC-34	191.110065	11.210609	1112 ± 33	22.839 ± 0.022	22.013 ± 0.020	0.825 ± 0.023	0.034
VCC2000GC-35	191.122260	11.178163	1087 ± 28	22.925 ± 0.038	21.779 ± 0.016	1.083 ± 0.035	0.034
VCC2000GC-36	191.116050	11.230333	1109 ± 20	20.599 ± 0.002	19.878 ± 0.006	0.629 ± 0.004	0.034
VCC2000GC-37	191.140260	11.163837	1189 ± 26	22.380 ± 0.012	21.439 ± 0.014	0.902 ± 0.016	0.034
VCC2000GC-38	191.138190	11.176321	1004 ± 38	21.193 ± 0.030	20.322 ± 0.026	0.792 ± 0.017	0.034
VCC2000GC-39	191.147055	11.198483	1149 ± 43	23.000 ± 0.026	22.169 ± 0.025	0.777 ± 0.023	0.034
VCC2000GC-40	191.146830	11.172589	970 ± 56	23.030 ± 0.033	22.174 ± 0.033	0.809 ± 0.024	0.034
VCC2000GC-41	191.155275	11.201397	1060 ± 14	21.365 ± 0.015	20.465 ± 0.011	0.851 ± 0.013	0.034
VCC2000GC-42	191.161890	11.205892	1086 ± 22	22.710 ± 0.037	21.815 ± 0.026	0.843 ± 0.031	0.034
VCC2000GC-43	191.167455	11.181426	942 ± 37	22.561 ± 0.010	21.812 ± 0.028	0.658 ± 0.019	0.034
			VCC 1062				
VCC1062GC-01	187.040970	9.794455	683 ± 12	22.890 ± 0.020	21.534 ± 0.020	1.325 ± 0.023	0.022
VCC1062GC-02	187.000530	9.817132	444 ± 19	21.895 ± 0.013	20.964 ± 0.013	0.886 ± 0.014	0.022
VCC1062GC-03	187.004025	9.816408	512 ± 23	22.575 ± 0.045	21.757 ± 0.062	0.729 ± 0.060	0.022
VCC1062GC-04	186.995685	9.807220	306 ± 18	24.395 ± 0.038	23.127 ± 0.057	1.231 ± 0.059	0.022
VCC1062GC-05	186.999240	9.805346	518 ± 15	21.978 ± 0.024	21.020 ± 0.018	0.902 ± 0.022	0.022
VCC1062GC-06	186.989805	9.792907	342 ± 21	22.503 ± 0.029	21.568 ± 0.029	0.859 ± 0.023	0.022
VCC1062GC-07	186.991335	9.802511	229 ± 30	23.130 ± 0.020	22.134 ± 0.022	0.980 ± 0.023	0.022
VCC1062GC-08	186.985650	9.798775	326 ± 21	22.977 ± 0.016	21.823 ± 0.026	1.109 ± 0.020	0.022
VCC1062GC-09	187.012260	9.817571	421 ± 21	22.418 ± 0.012	21.570 ± 0.025	0.791 ± 0.017	0.022
VCC1062GC-10	187.009785	9.810227	417 ± 21	22.582 ± 0.021	21.196 ± 0.017	1.305 ± 0.023	0.022
VCC1062GC-11	187.017090	9.809849	619 ± 18	22.279 ± 0.023	21.295 ± 0.017	0.908 ± 0.020	0.022
VCC1062GC-12	187.026240	9.811627	595 ± 23	21.870 ± 0.032	20.928 ± 0.051	0.805 ± 0.021	0.022
VCC1062GC-13	187.025115	9.796717	679 ± 20	21.588 ± 0.025	20.716 ± 0.038	0.778 ± 0.017	0.022
VCC1062GC-14	187.037430	9.792029	516 ± 13	21.699 ± 0.017	20.740 ± 0.012	0.914 ± 0.020	0.022
VCC1062GC-15	187.030080	9.811315	547 ± 18	22.869 ± 0.026	21.944 ± 0.024	0.891 ± 0.021	0.022
VCC1062GC-16	187.047585	9.805256	583 ± 17	22.437 ± 0.021	21.309 ± 0.016	1.088 ± 0.021	0.022
VCC1062GC-17	187.044615	9.816442	301 ± 25	22.926 ± 0.020	21.979 ± 0.015	0.900 ± 0.022	0.022
VCC1062GC-18	187.054260	9.809342	645 ± 21	23.102 ± 0.038	21.681 ± 0.027	1.413 ± 0.025	0.022
VCC1062GC-19	187.000560	9.796535	380 ± 19	22.458 ± 0.039	20.965 ± 0.037	1.487 ± 0.020	0.022
VCC1062GC-20	187.005885	9.798541	472 ± 17	22.254 ± 0.049	20.662 ± 0.061	1.482 ± 0.033	0.022
VCC1062GC-21	186.994635	9.807293	309 ± 21	22.574 ± 0.020	21.113 ± 0.018	1.414 ± 0.022	0.022
VCC1062GC-22	187.003020	9.802365	279 ± 11	21.228 ± 0.017	20.009 ± 0.020	1.165 ± 0.019	0.022
VCC1062GC-23	186.999375	9.790121	234 ± 18	23.134 ± 0.033	22.105 ± 0.017	1.038 ± 0.030	0.022

Table 8
(Continued)

| ID | R.A.(J2000) | Decl.(J2000) | v_{los} | g | z | $g - z$ | $E(B - V)$ |
| | (deg) | (deg) | (km s^{-1}) | (mag) | (mag) | (mag) | (mag) |
(1)	(2)	(3)	(4)	(5)	(6)	(7)	(8)
VCC1062GC-24	186.986835	9.806428	311 ± 14	22.979 ± 0.016	21.892 ± 0.028	1.094 ± 0.019	0.022
VCC1062GC-25	187.014075	9.808210	461 ± 19	22.665 ± 0.033	21.234 ± 0.024	1.293 ± 0.017	0.022
VCC1062GC-26	187.018665	9.791675	486 ± 13	21.268 ± 0.019	20.328 ± 0.015	0.859 ± 0.019	0.022
VCC1062GC-27	187.012890	9.792312	310 ± 18	22.946 ± 0.019	21.573 ± 0.021	1.289 ± 0.020	0.022
VCC1062GC-28	187.028310	9.813976	605 ± 19	22.592 ± 0.020	21.547 ± 0.017	0.991 ± 0.018	0.022
VCC1062GC-29	187.037685	9.798342	743 ± 19	21.771 ± 0.058	20.911 ± 0.051	0.866 ± 0.016	0.022
VCC1062GC-30	187.025085	9.798357	488 ± 57	23.113 ± 0.030	22.145 ± 0.051	0.866 ± 0.037	0.022
VCC1062GC-31	187.050615	9.787901	648 ± 17	22.409 ± 0.009	21.621 ± 0.021	0.718 ± 0.015	0.022
VCC1062GC-32	187.067940	9.802051	567 ± 11	21.506 ± 0.004	20.749 ± 0.010	0.720 ± 0.007	0.022
VCC1062GC-33	187.004535	9.801900	281 ± 12	24.777 ± 0.062	23.460 ± 0.066	1.271 ± 0.068	0.022
VCC1062GC-34	187.011405	9.804032	401 ± 11	21.189 ± 0.016	20.091 ± 0.020	1.012 ± 0.016	0.022
VCC1062GC-35	187.018740	9.803278	569 ± 24	21.804 ± 0.017	20.602 ± 0.019	1.157 ± 0.021	0.022
VCC1062GC-36	187.026120	9.804276	717 ± 18	22.399 ± 0.021	21.325 ± 0.021	1.002 ± 0.024	0.022
VCC1062GC-37	187.023465	9.805268	414 ± 23	22.974 ± 0.022	21.496 ± 0.045	1.366 ± 0.030	0.022
VCC1062GC-38	187.036740	9.806686	757 ± 15	22.842 ± 0.027	21.257 ± 0.025	1.534 ± 0.033	0.022
VCC1062GC-39	187.001925	9.804249	336 ± 10	20.526 ± 0.020	19.357 ± 0.023	1.111 ± 0.023	0.022
VCC1062GC-40	186.992850	9.808851	287 ± 18	22.179 ± 0.008	21.139 ± 0.014	0.991 ± 0.011	0.022
			VCC 685				
VCC685GC-01	185.989590	16.651251	1341 ± 24	22.262 ± 0.008	21.616 ± 0.026	0.609 ± 0.017	0.028
VCC685GC-02	185.959680	16.679079	1334 ± 27	22.130 ± 0.021	21.205 ± 0.014	0.868 ± 0.019	0.028
VCC685GC-03	185.975325	16.684580	1422 ± 22	21.954 ± 0.014	20.998 ± 0.011	0.897 ± 0.016	0.028
VCC685GC-04	185.978040	16.679291	1285 ± 31	22.256 ± 0.014	21.422 ± 0.017	0.754 ± 0.017	0.028
VCC685GC-05	185.988135	16.683411	918 ± 42	22.367 ± 0.021	21.238 ± 0.022	1.021 ± 0.016	0.028
VCC685GC-06	185.985465	16.692770	1025 ± 23	21.566 ± 0.019	20.658 ± 0.017	0.844 ± 0.010	0.028
VCC685GC-07	185.989155	16.688009	1062 ± 28	21.987 ± 0.026	21.125 ± 0.018	0.811 ± 0.024	0.028
VCC685GC-08	185.989965	16.701780	1168 ± 14	21.484 ± 0.021	20.311 ± 0.013	1.115 ± 0.023	0.028
VCC685GC-09	185.991735	16.694599	1588 ± 17	21.529 ± 0.012	20.532 ± 0.018	0.903 ± 0.017	0.028
VCC685GC-10	185.994150	16.696199	1520 ± 38	21.916 ± 0.023	20.950 ± 0.028	0.910 ± 0.018	0.028
VCC685GC-11	185.991225	16.709190	1343 ± 21	20.597 ± 0.018	19.737 ± 0.012	0.811 ± 0.006	0.028
VCC685GC-12	185.997015	16.701620	1178 ± 22	21.662 ± 0.016	20.724 ± 0.012	0.878 ± 0.020	0.028
VCC685GC-13	185.996025	16.711010	1208 ± 15	21.145 ± 0.015	19.992 ± 0.012	1.084 ± 0.017	0.028
VCC685GC-14	186.006900	16.716101	925 ± 33	22.649 ± 0.019	21.725 ± 0.015	0.871 ± 0.021	0.028
VCC685GC-15	186.000240	16.730289	1098 ± 31	21.078 ± 0.003	20.493 ± 0.012	0.508 ± 0.008	0.028

Note. Column (1): Object ID; Column (2): Right ascension in decimal degrees (J2000); Column (3): Declination in decimal degrees (J2000); Column (4): Heliocentric radial velocity and uncertainty; Columns.(5,6): g and z band magnitudes from the ACSVCS and NGVS (not corrected for Galactic extinction); Column (7): $g - z$ color; Column (8): The Galactic reddening determined by Schlegel et al. (1998). The corrections for foreground reddening were taken to be $A_g = 3.634E(B - V)$ and $A_z = 1.485E(B - V)$ in the g and z bands, respectively (Jordán et al. 2004).

parameter defined by Emsellem et al. (2007) to distinguish fast and slow rotators based on SAURON data within $1R_e$. The expression for λ is given by:

$$\lambda = \frac{\sum R_i F_i |V_i|}{\sum R_i F_i \sqrt{V_i^2 + \sigma_i^2}} \qquad (8)$$

where F_i, R_i, V_i, and σ_i are the flux, radius, velocity, and velocity dispersion in the ith bin, respectively. Emsellem et al. (2011) define the dividing line between slow and fast rotators at

$$\lambda = 0.31 \times \sqrt{\epsilon} \qquad (9)$$

where ϵ is the ellipticity of the system. However, Emsellem et al. (2011)'s IFU study of ETG specific angular momentum was generally limited to stars within $\lesssim 1R_e$.

Unlike for filled IFU observations, our GC and GDL data only sparsely sample the outer halos of our sample galaxies. The density of our data, therefore, is not an exact representation of the true density of the GC or stars. Therefore, rather than sum over the full 2D velocity field, which we do not have, we calculate λ in one-dimension as follows. (1) Through our kinematic fitting, we obtain the rotation velocity and velocity dispersion profile with radius. This is done in elliptical annuli whose ellipticities are alternately set to two values: zero and the mean ellipticity of the stars. (2) For every bin in radius, we replace F_i in Equation (8) with the number of GCs expected at that radius, and use the rotation velocity at that radius. We call the λ calculated in this way λ_{1D}. There is certainly a bias in using a one-dimensional (1D) method compared to λ calculated with full 2D data (which we now call λ_{2D}). This bias is due to the fact that the 1D method assigns the peak velocity amplitude to every position at a given radius. In reality, the velocity along the minor axis will be smaller than along the major axis. We can calibrate this bias, however, by comparing λ_{1D} and λ_{2D} for galaxies where we have full IFU coverage. To do this, we apply our 1D method to the 260 ETG galaxies from ATLAS^{3D}. The result is shown in Figure 17. We

Table 9
Galaxy Diffuse Light

ID	R.A.(J2000)	Decl.(J2000)	v_{los}	σ_{los} (km
	(deg)	(deg)	(km s^{-1})	s^{-1})
(1)	(2)	(3)	(4)	(5)
VCC 1231				
VCC1231GDL-01	187.450515	13.431453	2188 ± 14	174 ± 4
VCC1231GDL-02	187.447620	13.429241	2205 ± 18	208 ± 4
VCC1231GDL-03	187.453365	13.425970	2244 ± 12	153 ± 4
VCC1231GDL-04	187.456470	13.424834	2270 ± 14	157 ± 5
VCC1231GDL-05	187.457610	13.433330	2252 ± 14	154 ± 5
VCC1231GDL-06	187.447410	13.432945	2193 ± 14	185 ± 5
VCC1231GDL-07	187.450110	13.433290	2191 ± 14	163 ± 3
VCC1231GDL-08	187.445190	13.432550	2206 ± 14	189 ± 2
VCC1231GDL-09	187.444185	13.431620	2200 ± 18	197 ± 5
VCC1231GDL-10	187.441245	13.429025	2215 ± 18	204 ± 5
VCC1231GDL-11	187.442595	13.426672	2209 ± 16	195 ± 5
VCC1231GDL-12	187.461540	13.434665	2251 ± 16	165 ± 6
VCC1231GDL-13	187.463295	13.427741	2250 ± 15	203 ± 3
VCC1231GDL-14	187.468185	13.430573	2244 ± 17	197 ± 6
VCC1231GDL-15	187.468155	13.427391	2249 ± 17	196 ± 5
VCC1231GDL-16	187.473540	13.428547	2225 ± 25	186 ± 11
VCC1231GDL-17	187.438560	13.435633	2229 ± 22	211 ± 10
VCC1231GDL-18	187.475715	13.426306	2243 ± 29	⋯
VCC1231GDL-19	187.469025	13.435520	2239 ± 25	⋯
VCC1231GDL-20	187.434585	13.434356	2203 ± 17	⋯
VCC1231GDL-21	187.437780	13.422738	2217 ± 24	⋯
VCC1231GDL-22	187.428810	13.436997	2257 ± 29	⋯
VCC1231GDL-23	187.429695	13.433433	2200 ± 20	⋯
VCC1231GDL-24	187.429515	13.423301	2206 ± 24	⋯
VCC1231GDL-25	187.451670	13.442974	2210 ± 26	⋯
VCC1231GDL-26	187.465260	13.417413	2265 ± 32	⋯
VCC 2000				
VCC2000GDL-01	191.134440	11.189226	1032 ± 12	142 ± 3
VCC2000GDL-02	191.131935	11.189683	1144 ± 12	145 ± 3
VCC2000GDL-03	191.138505	11.193366	1034 ± 10	138 ± 7
VCC2000GDL-04	191.129370	11.193860	1115 ± 10	129 ± 6
VCC2000GDL-05	191.125890	11.190406	1166 ± 11	138 ± 9
VCC2000GDL-06	191.123100	11.191837	1139 ± 12	149 ± 12
VCC2000GDL-07	191.127015	11.186158	1109 ± 13	115 ± 10
VCC2000GDL-08	191.130135	11.184649	1094 ± 16	126 ± 10
VCC2000GDL-09	191.133315	11.183667	1065 ± 16	118 ± 8
VCC2000GDL-10	191.138505	11.193366	1034 ± 9	⋯
VCC2000GDL-11	191.119665	11.189951	1134 ± 17	⋯
VCC2000GDL-12	191.146710	11.191358	996 ± 28	⋯
VCC2000GDL-13	191.141985	11.195713	1067 ± 21	⋯
VCC2000GDL-14	191.140995	11.196223	1058 ± 20	⋯
VCC2000GDL-15	191.135130	11.198518	1057 ± 16	⋯
VCC2000GDL-16	191.131050	11.197987	1075 ± 19	⋯
VCC2000GDL-17	191.143635	11.196664	1040 ± 25	⋯
VCC2000GDL-18	191.146065	11.194601	1029 ± 26	⋯
VCC2000GDL-19	191.145060	11.197882	995 ± 33	⋯
VCC2000GDL-20	191.119545	11.199561	1052 ± 44	⋯
VCC2000GDL-21	191.119845	11.183841	1080 ± 42	⋯
VCC 1062				
VCC1062GDL-01	187.018740	9.803278	611 ± 17	172 ± 3
VCC1062GDL-02	187.026120	9.804276	683 ± 11	128 ± 6

Table 9
(Continued)

ID	R.A.(J2000)	Decl.(J2000)	v_{los}	σ_{los} (km
	(deg)	(deg)	(km s^{-1})	s^{-1})
(1)	(2)	(3)	(4)	(5)
VCC1062GDL-03	187.023465	9.805268	640 ± 12	123 ± 4
VCC1062GDL-04	187.014075	9.808210	486 ± 11	110 ± 5
VCC1062GDL-05	187.011405	9.804032	419 ± 12	136 ± 20
VCC1062GDL-06	187.017090	9.809849	531 ± 12	116 ± 7
VCC1062GDL-07	187.009785	9.810227	468 ± 14	115 ± 10
VCC1062GDL-08	187.026240	9.811627	613 ± 19	133 ± 12
VCC1062GDL-09	187.030080	9.811315	640 ± 15	120 ± 14
VCC1062GDL-10	187.036740	9.806686	799 ± 10	100 ± 7
VCC1062GDL-11	187.025115	9.796717	606 ± 11	138 ± 10
VCC1062GDL-12	187.025085	9.798357	610 ± 10	116 ± 7
VCC1062GDL-13	187.000560	9.796535	386 ± 10	120 ± 9
VCC1062GDL-14	187.005885	9.798541	385 ± 11	101 ± 8
VCC1062GDL-15	187.004535	9.801900	350 ± 11	111 ± 6
VCC1062GDL-16	187.001925	9.804249	346 ± 10	104 ± 5
VCC1062GDL-17	187.003020	9.802365	333 ± 9	102 ± 6
VCC1062GDL-18	186.999240	9.805346	356 ± 12	⋯
VCC1062GDL-19	186.995685	9.807220	352 ± 10	⋯
VCC1062GDL-20	186.994635	9.807293	362 ± 10	⋯
VCC1062GDL-21	187.037685	9.798342	665 ± 12	⋯
VCC1062GDL-22	186.992850	9.808851	382 ± 11	⋯
VCC1062GDL-23	186.991335	9.802511	340 ± 10	⋯
VCC1062GDL-24	186.986835	9.806428	381 ± 12	⋯
VCC1062GDL-25	186.985650	9.798775	376 ± 19	⋯
VCC1062GDL-26	187.012890	9.792312	501 ± 19	⋯
VCC1062GDL-27	187.028310	9.813976	608 ± 17	⋯
VCC1062GDL-28	187.018665	9.791675	527 ± 25	⋯
VCC1062GDL-29	187.012260	9.817571	572 ± 25	⋯
VCC 685				
VCC685GDL-01	185.985465	16.692770	1224 ± 34	129 ± 27
VCC685GDL-02	185.988135	16.683411	1042 ± 11	99 ± 12
VCC685GDL-03	185.997015	16.701620	1381 ± 12	94 ± 7
VCC685GDL-04	185.994150	16.696199	1372 ± 12	103 ± 7
VCC685GDL-05	185.989155	16.688009	1034 ± 12	102 ± 9
VCC685GDL-06	185.991735	16.694599	1278 ± 12	136 ± 9
VCC685GDL-07	185.978040	16.679291	1060 ± 90	⋯
VCC685GDL-08	185.989965	16.701780	1323 ± 71	⋯

Note. Column (1): Slit ID; Column (2): Right ascension in decimal degrees (J2000); Column (3): Declination in decimal degrees (J2000); Column (4): Heliocentric radial velocity and uncertainty; Column (5): Velocity dispersion and uncertainty.

can see that, as expected, λ_{1D} is generally overestimated compared to λ_{2D}. However, they follow a well-defined relation described as:

$$\lambda_{2D} \approx 0.82 \times \lambda_{1D}. \tag{10}$$

A similar relation was also found between the SAURON IFU data and long-slit (V/σ) measurements (Cappellari et al. 2007), and in the long-slit studies of λ in early-type dwarf galaxies (Toloba et al. 2015a). Our scaling factor is

larger than the value found by Toloba et al. (2015a) due to the fact that all of their long-slit data is along the major axis.

We apply this 1D method to the GC data in our Gemini sample. We also include six galaxies with GC data from the literature (Table 6). The uncertainties are determined from Monte Carlo simulations. Because the ellipticity of the GC system is not easily measured, we consider two cases, one where the ellipticity of the GC system is zero, and one where it is equal to that of the stars. The GC results are listed in Table 6 and Table 7. In practice, the difference is small between these two cases, and our results are not dependent on the assumed ellipticity of the GC system. In Figure 18, we compare λ_{1D} of GC (blue circles) and SAURON data (red circles) with ellipticity. In all cases, we use the ellipticity of the stars. Although this is potentially an issue, studies of the GC systems of ETGs in this mass range show that there is some correlation between the overall shape of GC systems and the ellipticity of the stellar distribution (Wang et al. 2013). The dashed lines link the same galaxy. The criterion of dividing slow and fast rotator with Equation (9) is rescaled by a factor 0.82 and plotted with a solid black line.

The three stellar slow rotators (red points below the line), are massive ETGs (NGC 4486, 4472, and 4636), and their GCs also are relatively slowly rotating, with $\lambda_{1D,GC} \sim 0.2$. Massive ETGs may experience multiple mergers with different orbital configurations and mass ratio, and this leads to aggregate slow rotation in the halo. However, there are also cases of massive ETGs that have significant rotation in their outer regions even though the galaxies are classified as slow rotators (e.g. NGC 1407, Romanowsky et al. 2009; Pota et al. 2013 and NGC 5128 Peng et al. 2004b). This case can be explained by angular momentum transfer to the outer regions by mergers.

For stellar fast rotators, however, the range in $\lambda_{1D,GC}$ is large. The most obvious examples are our three intermediate luminosity galaxies, where $\lambda_{1D,GC}$ of VCC 1062, 2000, and 1231 is 0.9, 0.3, and 0.1, respectively. Half of stellar fast rotators show the λ_{1D} of GC are smaller than the λ_{1D} of star. Two stellar fast rotators (NGC 3379 and 4473) have $\lambda_{1D,GC} < 0.2$, which means their outer regions are rotating very slowly. Similar results are also found by studying V_{rot}/σ (see the Figures 19 and 20 in Pota et al. 2013). It seems that, at least for the less massive galaxies, GCs may be kinematically decoupled from the stars.

5.3. Stellar Kinematic Trends with Galactocentric Radius

ETGs at $z \sim 2$ appear to be smaller and more dense than present-day ETGs of similar mass (Daddi et al. 2005; Trujillo et al. 2007; Cenarro & Trujillo 2009; van Dokkum et al. 2010; Whitaker et al. 2012). A two phase model of galaxy assembly (Naab et al. 2009; Oser et al. 2010; Khochfar et al. 2011) has been used to explain these observations. In the "in situ" phase, dissipative processes such as gas-rich major mergers and fragmenting turbulent disks (Dekel et al. 2009; Ceverino et al. 2010) form the central region. In the "ex situ" phase, accreted stars from minor mergers expand a galaxy's outskirts. These two phases *may* create different kinematic components in ETGs, although it is not necessarily clear which component would have larger angular momentum. For example, the core region is likely to dissipate its angular momentum through violent relaxation, but a late binary merger can also imprint rotation in the inner regions (Cox et al. 2006; Bois et al. 2011; Moody et al. 2014). The steady

accretion processes in the outer region could create a dynamically hotter with low rotation, but could also imprint rotation if the accretion is anisotropic. However, if there are indeed two regimes of galaxy building, we may expect to see this expressed in the kinematics. Indeed, some observations have found different stellar kinematics between the inner and outer regions of ETGs (Coccato et al. 2009; Proctor et al. 2009; Arnold et al. 2014).

One of the more comprehensive and recent studies of ETG stellar kinematics at large radii is by Arnold et al. (2014). They studied stellar kinematics in 22 nearby ETGs out to 2–4R_e with multi-slit observations from the SLUGGS survey (Brodie et al. 2014). They found that galaxies classified as fast rotators based on data in their inner regions can show a range of λ profiles in their outer regions, suggesting that "the apparent unification of the elliptical and lenticular (S0) galaxy families in the ATLAS^{3D} survey may be a consequence of a limited field of view." We measure $\lambda_{1D,GDL}$ in the range of $\sim$1.5–3R_e, and compare this measurement to $\lambda_{1D,SAURON}$, which represents the specific angular momentum in the inner regions. As in Arnold et al. (2014), we also find that λ in the outer regions can differ from what is found in the inner regions.

When trying to put into context the angular momentum profiles of galaxies, however, it is also important to consider ellipticity profiles. A changing ellipticity with radius leads to different expectations for a galaxy's λ with radius. For example, it is not surprising that NGC 3377 shows a decrease in its λ profile (Arnold et al. 2014), as its stellar light also gets rounder with radius. In Figure 19, we plot our measurements of λ_{1D} for the SAURON and GDL data versus radius, and also show the corresponding ellipticity profile (ϵ), derived from NGVS imaging (Ferrarese et al. 2012). For each galaxy's λ_{1D} profile, the solid and dotted lines represent the SAURON and GDL data, respectively. Both lines are cumulative λ_{1D} profiles with radius, but each data set is treated independently to allow for comparison (i.e., the GDL profile does not include the SAURON data).

Each of the three galaxies exhibits different characteristics. In VCC 1231 (left, red), λ_{1D} clearly decreases even though the ellipticity increases. This is not what one expects for an anisotropic rotator at constant inclination. In VCC 2000 (center, green), the rotation declines as the galaxy gets rounder. In VCC 1062 (right, blue), the ellipticity is nearly constant, but the rotation is increasing with radius. It is clear that while these galaxies may have been selected to be similar, their kinematics are quite different.

Whether this supports a picture of "two-phase" formation is less clear. One expects continuous transitions from the inner to outer regions of galaxies that may not necessarily result from distinct mergers or formation episodes. Raskutti et al. (2014) have studied the stellar kinematics of 33 massive ETGs with IFU data out to 2–5R_e and do not find a distinct transition between the inner and outer regions. Most of their sample galaxies are very massive, however, and it is possible that different kinematics between inner and outer regions are more easily seen in less massive systems, which are likely to have undergone fewer mergers than their massive counterparts. Individual merger events in massive galaxies are therefore more likely to be smoothed out by the larger number of merger and accretion events.

6. CONCLUSIONS

We have presented a kinematical analysis of halo stars and GCs in four intermediate luminosity galaxies in the Virgo cluster, based on Gemini/GMOS observations. These observations push these kinds of studies to lower mass ranges than previously done. Our GDL and GC data extend out to $4R_e$ and $8–14R_e$, respectively. We compare the GCs with the stars, and also compare the stellar kinematics in the inner ($R \lesssim 1R_e$) and outer regions. Although the four galaxies in our sample are all uniformly classified as "fast rotators" by the ATLAS[3D] project, we find that these galaxies show a diversity of GC and stellar kinematics in their outer regions.

1. The GCs display a wide range of kinematic properties that in some galaxies follow the stars of their host galaxy, but in others do not. We see cases of nearly zero net rotation in the GCs (VCC 1231), rotation about a misaligned axis (VCC 2000), strong rotation (VCC 1062), and counter-rotation (VCC 685).

2. We calculate the specific angular momentum, λ, of the GCs for three galaxies in our sample as well as in six galaxies from the literature. We find that massive ETGs that are classified as stellar slow rotators in their inner $R \lesssim 1R_e$ by ATLAS[3D] also tend to have slowly rotating GC systems (although at least one counter-example exists in the literature). The GC systems of stellar fast rotators, however, display a wide range of λ. Some galaxies whose stars are rapidly rotating have slowly or only moderately rotating GC systems, and vice versa. We interpret this diversity as the consequence of the stochastic nature of merging processes in less massive galaxies.

3. We compare the specific angular momentum for stars in the inner ($R \lesssim 1R_e$) and outer ($1.5 \lesssim R \lesssim 3.0$) regions of three of our sample galaxies. In conjunction with the ellipticity profiles derived from deep imaging, we find that one of our galaxies (VCC 1231) has a λ profile that decreases despite increasing ellipticity with radius, which is not what is expected for a simple anisotropic rotator at fixed inclination. The other two galaxies show falling (VCC 2000) and rising (VCC 1062) λ profiles. Even in this small sample, we can see that the stellar kinematics of otherwise morphologically similar galaxies can exhibit a diversity of properties at larger radii.

The kinematic differences we and others have found between GCs and stars, and between the inner and outer regions, in intermediate luminosity ETGs are beginning to allow us to dissect the merging and accretion histories of normal galaxies. The complex array of properties we are finding shows that this kind of wide-field kinematic study of a larger sample of intermediate-mass galaxies will be needed to fully sample the parameter space of galaxy assembly.

APPENDIX
UNSMOOTHED AND RAW VELOCITY FIELD

The unsmoothed and raw GC and stellar (GDL) velocity and velocity dispersion fields are shown in Figures 20 and 21. The rotation information we get from these figures is consistent with the smoothed and point symmetric velocity fields in Figures 5, 8, 11, and 14. Our quantitative analysis of specific angular momentum is based on the unsmoothed and non-symmetrized data.

The 2D velocity dispersion field of VCC 1231 shows good agreement with SAURON in the overlap region. Our result is also consistent with Foster et al. (2013) and Arnold et al. (2014), who find two velocity dispersion peaks at 3 kpc along the major axis. VCC 1231 is also called as "2σ" galaxy.

REFERENCES

Arnaboldi, M., Freeman, K. C., Gerhard, O., et al. 1998, ApJ, 507, 759
Arnold, J. A., Romanowsky, A. J., Brodie, J. P., et al. 2011, ApJL, 736, L26
Arnold, J. A., Romanowsky, A. J., & Brodie, J. P. 2014, ApJ, 791, 80
Bacon, R., Copin, Y., Monnet, G., et al. 2001, MNRAS, 326, 23
Bergond, G., Zepf, S. E., Romanowsky, A. J., Sharples, R. M., & Rhode, K. L. 2006, A&A, 448, 155
Blakeslee, J. P., Jordán, A., Mei, S., et al. 2009, ApJ, 694, 556
Bois, M., Emsellem, E., Bournaud, F., et al. 2011, MNRAS, 416, 1654
Brodie, J. P., Romanowsky, A. J., Strader, J., et al. 2014, ApJ, 796, 52
Bundy, K., Bershady, M. A., Law, D. R., et al. 2015, ApJ, 798, 7
Cappellari, M., & Emsellem, E. 2004, PASP, 116, 138
Cappellari, M., Emsellem, E., Bacon, R., et al. 2007, MNRAS, 379, 418
Cappellari, M., Emsellem, E., Krajnović, D., et al. 2011, MNRAS, 413, 813
Cenarro, A. J., & Trujillo, I. 2009, ApJL, 696, L43

Ceverino, D., Dekel, A., & Bournaud, F. 2010, MNRAS, 404, 2151
Coccato, L., Gerhard, O., Arnaboldi, M., et al. 2009, MNRAS, 394, 1249
Cole, S., Norberg, P., Baugh, C. M., et al. 2001, MNRAS, 326, 255
Cote, P., Marzke, R. O., & West, M. J. 1998, ApJ, 501, 554
Côté, P., McLaughlin, D. E., Cohen, J. G., & Blakeslee, J. P. 2003, ApJ, 591, 850
Côté, P., Blakeslee, J. P., Ferrarese, L., et al. 2004, ApJS, 153, 223
Cox, T. J., Dutta, S. N., di Matteo, T., et al. 2006, ApJ, 650, 791
Daddi, E., Renzini, A., Pirzkal, N., et al. 2005, ApJ, 626, 680
Dekel, A., Sari, R., & Ceverino, D. 2009, ApJ, 703, 785
Douglas, N. G., Napolitano, N. R., Romanowsky, A. J., et al. 2007, ApJ, 664, 257
Emsellem, E., Cappellari, M., Peletier, R. F., et al. 2004, MNRAS, 352, 721
Emsellem, E., Cappellari, M., Krajnović, D., et al. 2007, MNRAS, 379, 401
Emsellem, E., Cappellari, M., Krajnović, D., et al. 2011, MNRAS, 414, 888
Emsellem, E., Krajnović, D., & Sarzi, M. 2014, MNRAS, 445, L79
Faifer, F. R., Forte, J. C., Norris, M. A., et al. 2011, MNRAS, 416, 155
Ferrarese, L., Côté, P., Jordán, A., et al. 2006, ApJS, 164, 334
Ferrarese, L., Côté, P., Cuillandre, J.-C., et al. 2012, ApJS, 200, 4
Ford, H. C., Bartko, F., Bely, P. Y., et al. 1998, Proc. SPIE, 3356, 234
Forestell, A. D., & Gebhardt, K. 2010, ApJ, 716, 370
Foster, C., Arnold, J. A., Forbes, D. A., et al. 2013, MNRAS, 442, 3544
Foster, C., Spitler, L. R., Romanowsky, A. J., et al. 2011, MNRAS, 415, 3393
Gerhard, O., Kronawitter, A., Saglia, R. P., & Bender, R. 2001, AJ, 121, 1936
Guérou, A., Emsellem, E., McDermid, R., et al. 2015, ApJ, 804, 70
Hoffman, L., Cox, T. J., Dutta, S., & Hernquist, L. 2010, ApJ, 723, 818
Hook, I. M., Jørgensen, I., Allington-Smith, J. R., et al. 2004, PASP, 116, 425
Hwang, H. S., Lee, M. G., Park, H. S., et al. 2008, ApJ, 674, 869
Jarrett, T. H., Chester, T., Cutri, R., et al. 2000, AJ, 119, 2498
Jordán, A., Blakeslee, J. P., Peng, E. W., et al. 2004, ApJS, 154, 509
Jordán, A., McLaughlin, D. E., Côté, P., et al. 2007, ApJS, 171, 101
Jordán, A., Peng, E. W., Blakeslee, J. P., et al. 2009, ApJS, 180, 54
Khochfar, S., Emsellem, E., Serra, P., et al. 2011, MNRAS, 417, 845
Kissler-Patig, M., & Gebhardt, K. 1998, AJ, 116, 2237
Krajnović, D., Emsellem, E., Cappellari, M., et al. 2011, MNRAS, 414, 2923
Mehlert, D., Saglia, R. P., Bender, R., & Wegner, G. 1998, A&A, 332, 33
Mehlert, D., Saglia, R. P., Bender, R., & Wegner, G. 2000, A&AS, 141, 449
Mei, S., Blakeslee, J. P., Côté, P., et al. 2007, ApJ, 655, 144
Moody, C. E., Romanowsky, A. J., Cox, T. J., Novak, G. S., & Primack, J. R. 2014, MNRAS, 444, 1475
Naab, T., Johansson, P. H., & Ostriker, J. P. 2009, ApJL, 699, L178
Oser, L., Ostriker, J. P., Naab, T., Johansson, P. H., & Burkert, A. 2010, ApJ, 725, 2312

Peng, E. W., Ford, H. C., & Freeman, K. C. 2004a, ApJ, 602, 705
Peng, E. W., Ford, H. C., & Freeman, K. C. 2004b, ApJ, 602, 685
Peng, E. W., Jordán, A., Côté, P., et al. 2006, ApJ, 639, 95
Pierce, M., Beasley, M. A., Forbes, D. A., et al. 2006, MNRAS, 366, 1253
Pinkney, J., Gebhardt, K., Bender, R., et al. 2003, ApJ, 596, 903
Pota, V., Forbes, D. A., Romanowsky, A. J., et al. 2013, MNRAS, 428, 389
Proctor, R. N., Forbes, D. A., Forestell, A., & Gebhardt, K. 2005, MNRAS, 362, 857
Proctor, R. N., Forbes, D. A., Romanowsky, A. J., et al. 2009, MNRAS, 398, 91
Puzia, T. H., Kissler-Patig, M., Thomas, D., et al. 2004, A&A, 415, 123
Puzia, T. H., Miller, B. W., Trancho, G., et al. 2013, AJ, 145, 164
Raskutti, S., Greene, J., & Murphy, J. 2014, ApJ, 786, 23
Rix, H.-W., Franx, M., Fisher, D., & Illingworth, G. 1992, ApJL, 400, L5
Romanowsky, A. J., Douglas, N. G., Arnaboldi, M., et al. 2003, Sci, 301, 1696
Romanowsky, A. J., Strader, J., Spitler, L. R., et al. 2009, AJ, 137, 4956
Sánchez, S. F., Kennicutt, R. C., Gil de Paz, A., et al. 2012, A&A, 538, A8
Sánchez-Blázquez, P., Peletier, R. F., Jiménez-Vicente, J., et al. 2006, MNRAS, 371, 703
Schuberth, Y., Richtler, T., Hilker, M., et al. 2010, A&A, 513, A52
Schuberth, Y., Richtler, T., Hilker, M., et al. 2012, A&A, 544, A115
Skrutskie, M. F., Cutri, R. M., Stiening, R., et al. 2006, AJ, 131, 1163
Spolaor, M., Forbes, D. A., Hau, G. K. T., Proctor, R. N., & Brough, S. 2008, MNRAS, 385, 667
Strader, J., Romanowsky, A. J., Brodie, J. P., et al. 2011, ApJS, 197, 33
Toloba, E., Guhathakurta, P., van de Ven, G., et al. 2014, ApJ, 783, 120
Toloba, E., Guhathakurta, P., Boselli, A., et al. 2015a, ApJ, 799, 172
Toloba, E., Li, B., Guhathakurta, P., et al. 2015b, ApJ, submitted
Tonry, J. L., Dressler, A., Blakeslee, J. P., et al. 2001, ApJ, 546, 681
Trujillo, I., Conselice, C. J., Bundy, K., et al. 2007, MNRAS, 382, 109
van Dokkum, P. G. 2001, PASP, 113, 1420
van Dokkum, P. G., Whitaker, K. E., Brammer, G., et al. 2010, ApJ, 709, 1018
Wang, Q., Peng, E. W., Blakeslee, J. P., et al. 2013, ApJ, 769, 145
Weijmans, A.-M., Cappellari, M., Bacon, R., et al. 2009, MNRAS, 398, 561
Wernli, F., Emsellem, E., & Copin, Y. 2002, A&A, 396, 73
Whitaker, K. E., Kriek, M., van Dokkum, P. G., et al. 2012, ApJ, 745, 179
Woodley, K. A., Gómez, M., Harris, W. E., Geisler, D., & Harris, G. L. H. 2010, AJ, 139, 1871
Wu, X., Gerhard, O., Naab, T., et al. 2014, MNRAS, 438, 2701
Zhang, H.-X., Peng, E. W., Côté, P., et al. 2015, ApJ, 802, 30